MNRAS **472,** 1915–1931 (2017)
Advance Access publication 2017 August 16

doi:10.1093/mnras/stx2065

Charting the parameter space of the global 21-cm signal

Aviad Cohen,[1⋆] Anastasia Fialkov,[2] Rennan Barkana[1,3,4,5] and Matan Lotem[1]

[1]*Raymond and Beverly Sackler School of Physics and Astronomy, Tel Aviv University, Tel Aviv 69978, Israel*
[2]*Harvard-Smithsonian Center for Astrophysics, Institute for Theory and Computation, 60 Garden Street, Cambridge, MA 02138, USA*
[3]*Sorbonne Universités, Institut Lagrange de Paris (ILP), Institut d'Astrophysique de Paris, UPMC Univ Paris 06/CNRS, Paris, France*
[4]*Department of Astrophysics, University of Oxford, Denys Wilkinson Building, Keble Road, Oxford OX1 3RH, UK*
[5]*Perimeter Institute for Theoretical Physics, 31 Caroline St N., Waterloo, ON N2L 2Y5, Canada*

Accepted 2017 August 8. Received 2017 August 6; in original form 2016 September 8

ABSTRACT

The early star-forming Universe is still poorly constrained, with the properties of high-redshift stars, the first heating sources and reionization highly uncertain. This leaves observers planning 21-cm experiments with little theoretical guidance. In this work, we explore the possible range of high-redshift parameters including the star formation efficiency and the minimal mass of star-forming haloes; the efficiency, spectral energy distribution and redshift evolution of the first X-ray sources; and the history of reionization. These parameters are only weakly constrained by available observations, mainly the optical depth to the cosmic microwave background. We use realistic semi-numerical simulations to produce the global 21-cm signal over the redshift range $z = 6$–40 for each of 193 different combinations of the astrophysical parameters spanning the allowed range. We show that the expected signal fills a large parameter space, but with a fixed general shape for the global 21-cm curve. Even with our wide selection of models, we still find clear correlations between the key features of the global 21-cm signal and underlying astrophysical properties of the high-redshift Universe, namely the Ly α intensity, the X-ray heating rate and the production rate of ionizing photons. These correlations can be used to directly link future measurements of the global 21-cm signal to astrophysical quantities in a mostly model-independent way. We identify additional correlations that can be used as consistency checks.

Key words: galaxies: formation – galaxies: high-redshift – intergalactic medium – cosmology: theory.

1 INTRODUCTION

Some of the most exciting epochs in cosmic history, including the cosmic dark ages, the formation of the first radiative sources (cosmic dawn) and the onset of the epoch of reionization during which the entire Universe became ionized, are currently inaccessible observationally. Our theoretical understanding of galaxy formation gives us significant guidance, but this is limited by astrophysical uncertainties (Barkana 2016). A major focus are three cosmic events expected at early times (Madau, Meiksin & Rees 1997): cosmic reionization [known to have occurred given the highly ionized Universe at present (Gunn & Peterson 1965)], cosmic heating (likely by X-rays) and Ly α coupling (an event specific to 21-cm cosmology).

In the hierarchical picture of structure formation, haloes grew gradually during the dark ages, assembling mass via gravitational interactions. Massive enough haloes were able to retain gas that could radiatively cool, condense and form stars, with the first stellar objects forming at $z \sim 65$ (Naoz & Barkana 2006; Fialkov et al. 2012). The minimal mass of haloes within which stars can form, $M_{\rm min}$, depends on the chemical composition of the gas, and in the pristine conditions at high redshifts, two cooling channels dominate: (1) radiative cooling of molecular hydrogen happens in the smallest haloes, with mass above $10^5\,{\rm M}_\odot$ (e.g. Tegmark et al. 1997; Bromm, Coppi & Larson 2002; Yoshida et al. 2003), and (2) radiative cooling of atomic hydrogen takes place in haloes with mass above $10^7\,{\rm M}_\odot$ (e.g. Barkana & Loeb 2001). Star formation in small haloes is a vulnerable process and is believed to be affected by several feedback mechanisms that can either boost or suppress the formation of the next generation of stars. One of the mechanisms discussed in the literature is the Lyman–Werner (LW) feedback. UV radiation in the LW band emitted by the first stars can dissociate hydrogen molecules (Haiman, Rees & Loeb 1997), depleting the reservoirs of gas available for the formation of the future stars (however, the efficiency of the LW feedback is poorly understood, e.g. Visbal et al. 2014; Schauer et al. 2015). Because LW photons reach up to ∼100 comoving Mpc, this feedback is not local and star formation activity at one site can potentially

⋆ E-mail: aviadc11@gmail.com

sterilize haloes over a large cosmological volume. Another possible feedback mechanism is the stellar feedback from supernova explosions that can expel gas from the halo, effectively increasing the minimum cooling mass well above the atomic cooling threshold (Wyithe & Loeb 2013). An additional feedback mechanism that can affect star formation is the photoheating feedback that becomes efficient once the intergalactic gas is photoheated above 10^4 K by ionizing radiation emitted by stars; this gas stops accreting on to haloes below $\sim 10^8$–10^9 $M_\odot$, thus quenching subsequent star formation within them. Because heavy haloes are rare at high redshifts, LW, supernova and photoheating feedbacks can, when they are effective, delay major cosmological events such as the heating of the intergalactic gas and reionization. Finally, there is a possibility that light haloes (below the atomic cooling mass) can continue to contribute to star formation even in the presence of LW radiation, via the metal-line cooling channel. Because metal-line cooling is more efficient than molecular cooling, this channel can dominate star formation in small haloes once the gas is enriched by the first supernovae explosions. However, the possibility of star formation via metal cooling in the early universe and its contribution to the total star formation is highly uncertain (e.g. Jeon et al. 2014; Wise et al. 2014; O'Shea et al. 2015; Cohen, Fialkov & Barkana 2016).

The fraction of gas that is converted into stars (the star formation efficiency, hereafter SFE) is another unknown and can be of order a few tens of per cent or lower depending on the halo mass, redshift and dominant feedback mechanisms. Observations at low redshifts show that the star formation efficiency is a few per cent in massive haloes (Tinker et al. 2017), while isolated dwarf galaxies show a very low SFE of the order of ∼0.1–0.01 per cent (Read et al. 2017). Simulations of high-redshift stellar activity present a large scatter of values for SFE, especially for small haloes that likely dominated the early Universe (e.g. Wise et al. 2014; O'Shea et al. 2015; Xu et al. 2016). Matching the observed luminosity function to the expected number of haloes at $z \gtrsim 6$ shows that the peak value of the SFE is 30 per cent for haloes of $M_\mathrm{h} \sim 10^{11}$–$10^{12}$ $M_\odot$, dropping to SFE ∼10 per cent at the low-mass $M_\mathrm{h} \sim 2 \times 10^{10}$ $M_\odot$ and high-mass $M_\mathrm{h} \sim 3 \times 10^{13}$ $M_\odot$ limits (Behroozi & Silk 2015; Mason, Trenti & Treu 2015; Mashian, Oesch & Loeb 2016; Sun & Furlanetto 2016; Mirocha, Furlanetto & Sun 2017).

As noted above, the formation of the first luminous objects had a dramatic effect on the Universe, completely changing the environment. The first astronomical objects emitted UV and X-ray radiation that heated and ionized the gas, while supernova explosions enriched the primordial gas with metals, leading to the formation of the next generation of stars. Stars are believed to have been the main origin of UV photons that reionized the neutral intergalactic medium (IGM), resulting in the total cosmic microwave background (CMB) optical depth of $\tau \sim 0.055 \pm 0.009$ (Planck Collaboration et al. 2016c). However, the origin of the first heating sources, which raised the temperature of the IGM above that of the CMB, is still debatable. The most plausible heating radiation is X-rays, which can travel far even in a neutral Universe. The X-ray efficiency of the sources as well as their spectral energy distribution (SED) remain very poorly constrained. Several different candidates have been proposed in the literature including X-ray binaries (XRBs; Mirabel et al. 2011), mini-quasars (Madau et al. 2004), hot gas in the first galaxies and hard X-rays produced via inverse Compton scattering of the CMB off electrons accelerated by supernovae (Oh 2001). Finally, there are more exotic possibilities such as dark matter annihilation (Cirelli, Iocco & Panci 2009). Out of the plethora of candidates, XRBs (which have a hard SED that peaks around 1–3 keV) are likely to be the dominant source of cosmic heating at $z \gtrsim 6$ (Mirabel et al. 2011; Fragos et al. 2013). The hard spectrum has a major effect on 21-cm cosmology, substantially delaying cosmic heating and decreasing the amplitude of 21-cm fluctuations from heating (Fialkov, Barkana & Visbal 2014). Extrapolations of recent observations to high redshift continue to support such a scenario (Madau & Fragos 2017; Mirocha et al. 2017). However, direct observational constraints on the X-ray efficiency of the first sources are rather weak. Upper limits on the heating efficiency come from the soft unresolved cosmic X-ray background (Fialkov et al. 2017) and lower limits are given by the observed upper limits on the 21-cm power spectrum (Ali et al. 2015; Pober et al. 2015; Fialkov et al. 2017).

The most promising tool to explore the early universe is the redshifted 21-cm signal of neutral hydrogen. It is strongly affected by astrophysics and cosmology, and, thus, is believed to be an excellent probe of processes that took place at high redshifts. In particular, the first stars also are expected to have emitted Ly α photons (plus higher energy photons that redshifted down to Ly α), which coupled the 21-cm line (in terms of the relative abundance of its ground and excited states) to the kinetic gas temperature, leading to a strong, potentially observable, 21-cm signal (Madau et al. 1997), which otherwise would have faded away by $z \sim 30$.

The currently unexplored parameter space of the early universe leaves a large window within which the 21-cm signal may fall, making it difficult to predict its shape and guide current and future radio telescopes. The signal has not been detected yet[1] and only upper limits have been placed on its power spectrum at redshift $z < 10$ (Ali et al. 2015; Pober et al. 2015; Ewall-Wice et al. 2016); however, many current and future observations aim to detect and measure the signal out to $z \sim 35$. Experiments such as the Experiment to Detect the Global EoR Step (EDGES; Bowman & Rogers 2010), the Shaped Antenna measurement of the background RAdio Spectrum (SARAS; Patra et al. 2013), the Large Aperture Experiment to Detect the Dark Age (LEDA; Bernardi, McQuinn & Greenhill 2015) and the Dark Ages Radio Explorer (DARE; Burns et al. 2012) are trying to measure the global signal, while the Low Frequency Array (LOFAR; van Haarlem et al. 2013), the Murchison Wide-field Array (MWA; Bowman et al. 2013; Ewall-Wice et al. 2016), the Precision Array to Probe the Epoch of Reionization (PAPER; Ali et al. 2015), the Hydrogen Epoch of Reionization Array (HERA; Pober et al. 2014; DeBoer et al. 2017) and the Square Kilometre Array (SKA; Koopmans et al. 2015) are aiming to measure the power spectrum.

Our goal in this paper is to explore the full parameter space of the global 21-cm signal resulting from the uncertainties in the astrophysical parameters of the high-redshift universe. Other recent work has focused on extrapolating low-redshift observations of galaxies to high redshift (Madau & Fragos 2017; Mirocha et al. 2017), but we adopt a more flexible approach. While it will be interesting to use observations to find out if such extrapolations are accurate, a priori, this cannot be assumed. Compared to current observations (which are mostly at relatively low redshift), conditions are very different at redshift 20, e.g. in terms of the CMB temperature, the cosmic and virial halo densities (of both the dark matter and gas), the typical mass of galactic haloes and halo merger histories. Thus,

[1] Bernardi et al. (2016) used a Bayesian method with a simplified Gaussian model for the absorption feature (see Section 2) to constrain the global signal using early LEDA observations.

the astrophysical properties of early galaxies could be quite different from those suggested by extrapolations of observed galaxies, and it is important to keep an open mind until direct observational evidence becomes available.

In what follows, as we lay out the large parameter space possible for the global 21-cm signal, we try to characterize the properties of this signal and find relations between the shape of the global signal and the astrophysical parameters at high redshifts. Mirocha, Harker & Burns (2013) previously addressed parameter reconstruction using a physical model for the global signal. In this (as well as the follow-up works by Mirocha, Harker & Burns 2015; Harker et al. 2016, where the authors study how well current and near-future experiments could constrain the four parameters of their model using the measurements of the signal's three key points and taking into account the foreground and the noise), the authors used analytical formulas or simple models that account only for the mean evolution of the Universe. In contrast, our more realistic simulations include spatial fluctuations in star formation and take into account the finite effective horizons of the radiative backgrounds, spatially inhomogeneous feedback processes and time delay effects. We also capture a wider parameter space, as our code includes the possibility of having substantial star formation in haloes below the atomic cooling threshold, in which case spatially inhomogeneous processes such as the streaming velocity and LW feedback play a key role (and are included in our 21-cm code but not in others).

This paper is organized as follows. In Section 2, we briefly discuss the general properties of the 21-cm signal as well as our numerical methods. We present and discuss our specific choice of the parameters and their ranges in Section 3, and show the resulting parameter space spun by the 21-cm signal in Section 4. Finally, we summarize our results and discuss our conclusions in Section 5.

2 SIMULATED 21-CM SIGNAL

In order to explore the parameter space of the early universe and produce a library of possible global 21-cm signals in the redshift range of $z = 6$–40, we use a semi-numerical approach (Mesinger, Furlanetto & Cen 2011; Visbal et al. 2012; Fialkov, Barkana & Visbal 2014). Our code is a combination of numerical simulation and analytical calculations and has enough flexibility to explore the large dynamical range of astrophysical parameters. We simulate large cosmological volumes of the universe (384^3 Mpc^3; all distances comoving unless indicated otherwise) with a 3 Mpc resolution, and the outcome of the simulation is the resulting inhomogeneous 21-cm signal which for our purposes in this paper we average over the box. In addition, inhomogeneous backgrounds of X-ray, Lyα, LW and ionizing radiation at every redshift are computed. In our simulation, the statistically generated initial conditions for structure formation, i.e. the density field and the supersonic relative velocity between dark matter and baryons (Tseliakhovich & Hirata 2010; Tseliakhovich, Barkana & Hirata 2011; Visbal et al. 2012), are linearly evolved from recombination to lower redshifts. Using the values of large-scale density and velocity in each cell, we apply the extended Press–Schechter formalism (Barkana & Loeb 2004; Press & Schechter 1974), as modified by the large-scale density fluctuations and the supersonic relative velocities, to calculate the local fraction of gas in collapsed structures in each pixel and at each redshift. We then populate each pixel with stars, given the star formation efficiency, as described in Section 3. To calculate the intensities of the various radiative backgrounds, we use the star formation rate (SFR), which is determined by the time derivative of the collapsed fraction and the SFE. We use the standard

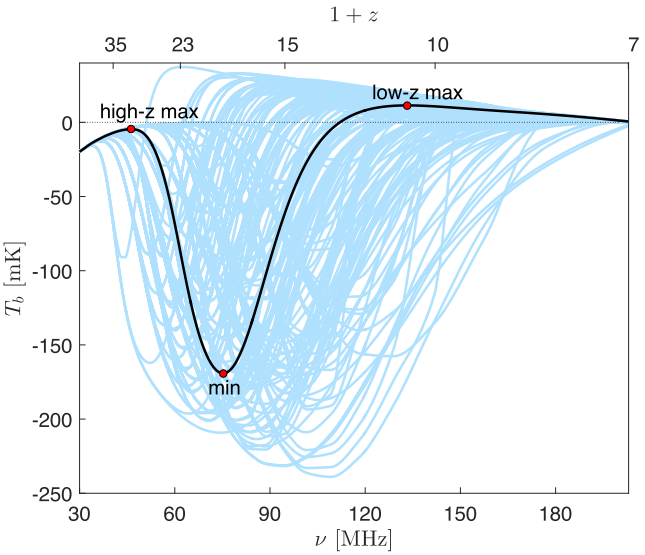

Figure 1. The 21-cm global signal as a function of redshift for our standard case (black line), with red points marking the three turning points (from left to right: the high-z maximum, the minimum and the low-z maximum). Light-blue lines show the entire set of realizations of the 21-cm signal for the 193 different astrophysical models discussed in this paper and summarized in Table 1. The full list of models appears in the Appendix.

spectra of Population II stars from Barkana & Loeb (2005b) (based on Leitherer et al. 1999) to determine the spectrum and intensity of Lyα and LW photons, the strong LW feedback from Fialkov et al. (2013) (when LW feedback is applied) and the standard cosmological parameters (Planck Collaboration et al. 2014). Star formation is also subject to the photoheating feedback (Sobacchi & Mesinger 2013; Cohen et al. 2016).

The observed cosmic mean 21-cm brightness temperature relative to the CMB can be expressed as (Madau, Meiksin & Rees 1997; Furlanetto, Oh & Briggs 2006; Barkana 2016)

$$T_{\rm b} = 26.8\, x_{\rm H\,I} \left(\frac{1+z}{10}\right)^{1/2} (1+\delta) \left[1 - \frac{T_{\rm CMB}}{T_S}\right] {\rm mK}, \quad (1)$$

where $x_{\rm H\,I}$ is the neutral hydrogen fraction, δ is the matter overdensity, $T_{\rm CMB}$ is the CMB temperature and T_S is the spin temperature, which can be expressed as

$$T_S^{-1} = \frac{T_{\rm CMB}^{-1} + x_c T_{\rm gas}^{-1} + x_\alpha T_c^{-1}}{1 + x_c + x_\alpha}. \quad (2)$$

Here, $T_{\rm gas}$ is the (kinetic) gas temperature, T_c is the effective (colour) Lyα temperature that is very close to $T_{\rm gas}$, and x_c and x_α are the coupling coefficients for collisions and Lyα scattering, respectively. In equation (1), we neglect the peculiar velocity term since in the global signal it averages out to linear order and adds only a tiny correction (Bharadwaj & Ali 2004; Barkana & Loeb 2005a).

A typical dependence of the sky-averaged signal ('the 21-cm global signal') on frequency is shown in Fig. 1 (black line, our standard case as will be explained below). Its characteristic structure of peaks and troughs encodes information about global cosmic events (Furlanetto 2006). At early times $z \gtrsim 40$ collisions between neutral hydrogen atoms and each other (and with other species) drive $T_S \to T_{\rm gas}$, and the signal is seen in absorption, because in the absence of heating sources $T_{\rm gas} < T_{\rm CMB}$. As the universe expands and cools, collisions become rare and hydrogen atoms are driven towards thermal

Table 1. Summary of the considered models. The name of the category of models appears in the first column, for reference. We vary the cooling channel (column 2), star formation efficiency (f_*, column 3), X-ray efficiency of X-ray sources (f_X, column 4), spectral energy distribution of X-ray sources (SED, column 5) and the total CMB optical depth (τ, column 6), taking various combinations of the various parameters within each category. For each cooling channel, we use all the possible combinations of the parameters f_*, f_X, SED and τ that are listed in the same category. Note that some of the parameter combinations are ruled out by PAPER measurements and/or they produce only very large $\tau > 0.098$ and thus fail our normalization criterion. These models are included here but are excluded from our results. Also, in the Fialkov et al. (2017) category, each case has a different lower and upper limit on f_X (see Section 3.2). A complete listing of the details of all the included models is given in the Appendix.

Category	Cooling channel	f_*	f_X	SED	τ
Standard case (1 model)	Atomic cooling	0.05	1	Hard SED	0.066
Small variations (32 models)	Molecular cooling Massive cooling	$0.05 \times \sqrt{10}$ $0.05/\sqrt{10}$	$\sqrt{10}$ $1/\sqrt{10}$	Hard SED & Mini-quasars Soft SED & Mini-quasars	0.066 0.082
Large variations (20 models)	Metal cooling Supermassive cooling	0.5 0.005	0.1 10	Soft SED Mini-quasars	0.066 0.098
Space filler (106 models)	Molecular cooling Atomic cooling Massive cooling	0.005 0.05 0.5	0.1 1 8	Soft SED Hard SED	0.066 0.082
Fialkov et al. (2017) (22 models)	Atomic cooling Massive cooling	0.05	lower limit 1 upper limit	Soft SED Hard SED Mini-quasars	$0.06 - 0.11$

equilibrium with the CMB; thus, the 21-cm brightness temperature (measured relative to the CMB temperature) decreases in magnitude and the signal nearly vanishes. When the luminous sources turn on significantly, the signal reaches a local maximum (still being observed in absorption). We refer to this point as the 'high-z maximum point', and it happens at $z \sim 30$ for our standard case (and is equivalent to the turning point B in the nomenclature of Mirocha et al. 2013). As the first sources of Ly α photons turn on, Ly α radiation begins to drive T_S to $T_c \sim T_{\rm gas}$ via the Wouthuysen-Field effect (Wouthuysen 1952; Field 1958). This transition normally occurs before many X-ray sources turn on and thus the signal is seen in absorption. Once Ly α coupling approaches saturation, and X-ray sources turn on significantly, the signal reaches its local minimum value, ~ -170 mK in our standard case. We refer to this point as the 'minimum point' (equivalent to turning point C of Mirocha et al. 2013), and it occurs at $z \sim 18$ for our standard case. At this time, the population of heating sources steadily increases and the contrast between $T_{\rm gas}$ and $T_{\rm CMB}$ decreases. As the X-ray sources heat the gas, if the gas temperature rises above that of the CMB, the 21-cm signal is seen in emission. As soon as reionization starts, the fraction of neutral gas decreases, thus decreasing the amplitude of the 21-cm signal. In most models (including our standard case), X-ray sources manage to heat the gas above the CMB temperature, and once heating saturates (i.e. reaches $T_{\rm gas} \gg T_{\rm CMB}$), another local maximum, the 'low-z maximum point' ($z \sim 10$, turning point D of Mirocha et al. 2013), is formed. The advance of reionization and decrease of redshift decrease the signal (see equation 1), until the end of reionization makes $x_{\rm H\,I} = 0$ and the signal vanishes (we neglect the small fraction of neutral gas left over inside galaxies). The three key points (within the relevant redshift range) in the evolution of the signal are marked with red dots in Fig. 1.

3 MODEL DETAILS AND PARAMETER RANGES

As discussed in the introduction, high-redshift astrophysical parameters such as the star formation efficiency, X-ray efficiency and SED, and feedback mechanisms are poorly constrained. However, they have a strong impact on the 21-cm signal, affecting the location and amplitude of the main features of the global signal. To survey possible realizations, we ran our simulation code for 193 different sets of astrophysical parameters chosen from the ranges described below, and analysed the properties of the global 21-cm signal in each case. Table 1 presents a brief summary of the considered models, while the full list of models and their parameter values is in the Appendix.

3.1 Star formation efficiency and cooling channel

The star formation efficiency is believed to vary with halo mass, redshift and metallicity of the gas, and it also depends on feedback mechanisms. It strongly affects the shape of the global 21-cm signal by influencing the amount of radiation produced by stars. For otherwise identical astrophysical parameters, a higher SFE implies an earlier onset of Ly α coupling, and a faster build-up of X-ray and ionizing radiation backgrounds. The 21-cm absorption feature is shallower than in the case of low SFE, because cosmic heating turns on earlier and the gas does not have as much time to cool down. As a function of the SFE, all the key points of the global 21-cm signal are shifted to lower (higher) frequencies in the case of a higher (lower) SFE.

The high-redshift value of the SFE in the small haloes where the first population of stars formed is highly unconstrained, due to the lack of direct observations. Existing simulations suggest relatively low values of the SFE, but show a large scatter (e.g. Wise et al. 2014; O'Shea et al. 2015; Xu et al. 2016). Based on the low-redshift observations, typical values of the SFE used in the literature are a few per cent (e.g. Furlanetto, Oh & Briggs 2006; Mesinger, Greig & Sobacchi 2016; Fialkov et al. 2017). However, not only is the typical value of the SFE uncertain, its dependence on halo mass at the low-mass end is unclear as well (Behroozi & Silk 2015; Mirocha et al. 2017; Mason 2015; Mashian 2016; Sun & Furlanetto 2016). Therefore, as in Cohen et al. (2016), we consider two possibilities for the SFE-$M_{\rm h}$ dependence: a sharp low-mass cut-off,

$$f_*(M) = \begin{cases} f_* & M_{\rm min} < M, \\ 0 & \text{otherwise}, \end{cases} \quad (3)$$

and a gradual low-mass cut-off (Machacek, Bryan & Abel 2001; Fialkov et al. 2013),

$$f_*(M) = \begin{cases} f_* & M_{\rm atomic} < M, \\ f_* \frac{\log(M/M_{\rm min})}{\log(M_{\rm atomic}/M_{\rm min})} & M_{\rm min} < M < M_{\rm atomic}, \\ 0 & \text{otherwise}, \end{cases} \quad (4)$$

where $M_{\rm min}$ is the minimum halo mass for star formation, $M_{\rm atomic}$ is the minimum halo mass for atomic cooling and f_* is a (constant) parameter that stands for the SFE at the high-mass end. Here, we use $f_* = 5$ per cent as our standard value while also adopting the values 0.5 per cent and 50 per cent when exploring the parameter space. Note that in both equations (3) and (4), the SFE-$M_{\rm h}$ dependence is flat for haloes above the atomic cooling threshold, though we also vary the minimum halo mass widely, including up to values well above this threshold.

The parameter $M_{\rm min}$ is determined either by the cooling channel through which stars can form, or by feedback. In the hierarchical picture of structure formation, low-mass haloes form at higher redshifts and are more numerous than high-mass haloes at early times. Therefore, in the cases with lower $M_{\rm min}$, stars form earlier, leading to an earlier Ly α coupling of the 21-cm signal to $T_{\rm gas}$ and shifting the location of the high-z maximum point to higher redshift.

As described in Section 1, high-redshift star formation could happen via several different channels, with each cooling mechanism having a different minimum cooling mass, which evolves with redshift. For simplicity, we use the minimum virial circular velocity, V_c, instead of the minimal cooling mass throughout this paper, since V_c is less strongly dependent on redshift (Barkana 2016). To probe different cooling and feedback mechanisms, we consider here five different scenarios:

(i) Molecular cooling haloes: In this case, stars can form in haloes with masses down to the cooling mass of molecular hydrogen, i.e. $V_c = 4.2\,{\rm km\,s^{-1}}$ which corresponds to $M_{\rm vir} \approx 7 \times 10^5\,{\rm M_\odot}$ at $z = 20$ if LW feedback is turned off. In all cases with molecular cooling, we include LW feedback and star formation efficiency with the gradual low-mass cut-off (equation 4).

(ii) Metal cooling haloes: This is same as molecular cooling haloes but without LW, which does not significantly affect the cooling of metal-rich gas, and with star formation efficiency with the sharp low-mass cut-off (equation 3), to obtain the maximal effect (this is the 'Maximal' case from Cohen et al. 2016). We note that all cases with small haloes are significantly affected by the supersonic streaming velocity, which significantly and inhomogeneously suppresses star formation, while haloes above the atomic cooling are only weakly affected by it (Tseliakhovich & Hirata 2010; Tseliakhovich et al. 2011; Visbal et al. 2012).

(iii) Atomic cooling haloes: Stars form in haloes with masses down to the cooling threshold of atomic hydrogen, i.e. with $V_c = 16.5\,{\rm km\,s^{-1}}$ (corresponds to $M_{\rm vir} \approx 3 \times 10^7\,{\rm M_\odot}$ at $z = 20$).

(iv) Massive haloes: Stars formation occurs in haloes with masses down to $10 \times M_{\rm atomic}$ that corresponds to $V_c = 35.5\,{\rm km\,s^{-1}}$.

(v) Supermassive haloes: Stars form in haloes with masses down to $100 \times M_{\rm atomic}$ ($V_c = 76.5\,{\rm km\,s^{-1}}$). This or the previous case might correspond to strong supernova feedback that expels all the gas out of low-mass haloes.

3.2 X-ray SED and normalization

X-ray heating strongly affects the expected global 21-cm signal by affecting the depth and the location of the absorption trough, i.e. the minimum point, as well as the subsequent rise towards an emission signal. More efficient X-ray sources imply a shallower absorption trough with its location shifted to higher redshift, plus a higher emission signal at the low-z maximum point. On the other hand, weaker heating results in a deeper trough shifted to lower redshift, with a suppressed or vanishing emission signal. The energy that goes into heating of the IGM depends on the total X-ray energy emitted in the band ∼0.2–10 keV. Photons with lower energies are absorbed locally by dust in the star-forming region, while more energetic photons have such long mean-free-paths that they lose their energy to redshift effects and some are not absorbed even by the end of reionization. The photons that produce early cosmic heating might also contribute to the unresolved soft X-ray background observed by *Chandra* (Lehmer et al. 2012), which can be used to put upper limits on the efficiency of X-ray sources (Fialkov et al. 2017).

As mentioned in the introduction, the most plausible sources for dominating high-redshift X-ray emission are XRBs. They are expected to have a hard X-ray SED that peaks at about 1–3 keV and is nearly independent of redshift. We adopt the hard SED case from Fragos et al. (2013); Fialkov et al. (2014) to describe the spectral shape of XRBs. Another category of possible X-ray sources that we consider here are mini-quasars. Because their hard SED is similar in shape to that of XRBs, with only a weak dependence on the black hole mass and redshift (Tanaka et al. 2012), we adopt the same shape of SED for mini-quasars as for the XRBs for simplicity. In order to cover a wide range of SEDs, we also consider the possibility of a soft power-law spectrum, which is often used in the literature (Furlanetto 2006; Mesinger et al. 2011). The main difference between the soft and the hard SEDs is that in the latter case the typical mean free path of X-ray photons is much larger, so there is a long delay in the energy absorption; the delay causes energy loss due to redshift effects, so that the total absorbed energy is reduced by a factor of ∼5 compared to the soft case (Fialkov et al. 2014; Fialkov & Barkana 2014); furthermore, hard sources at high redshifts tend to contribute more photons within the energy range corresponding to the observed soft X-ray background (Fialkov et al. 2017).

To calculate the total X-ray luminosity, we use the observed SFR$-L_X$ relation:

$$\frac{L_X}{\rm SFR} = 3 \times 10^{40} f_X {\rm erg\,s^{-1}\,M_\odot^{-1}\,yr}, \quad (5)$$

where L_X is the bolometric luminosity summed over 0.2–95 keV and f_X is the X-ray efficiency of sources (assumed to be constant). This relation is based on observations of nearby starburst galaxies and XRBs (Grimm, Gilfanov & Sunyaev 2003; Gilfanov, Grimm & Sunyaev 2004; Mineo, Gilfanov & Sunyaev 2012), and the standard normalization for XRBs (with $f_X = 1$) includes an order-of-magnitude increase in this ratio at the low metallicity expected for high-redshift galaxies (Fragos et al. 2013). In any case, we try a wide range of values of f_X, so for us equation (5) is just a fiducial value. We use equation (5) for the cases of a hard or soft spectrum, and in the case of mini-quasars, we add to it the ratio between the X-ray luminosity of XRBs (assumed given by equation 5) and that of mini-quasars (Wyithe & Loeb 2003; Fialkov et al. 2014, 2017):

$$\frac{L_{\rm MQ}}{L_{\rm XRB}} \sim 0.1 \left(\frac{0.05}{f_*}\right) \left(\frac{M_{\rm halo}}{10^8\,{\rm M_\odot}}\right)^{2/3} \left(\frac{1+z}{10}\right). \quad (6)$$

The additional dependence of the mini-quasar luminosity on the halo mass results in a relatively small contribution from these sources at redshifts $z \gg 8$, when halo masses are typically small, but they become dominant (when mixed together with other sources)

at lower redshift, when larger haloes form. Note that the luminosity of mini-quasars includes the factor f_X as well; in cases that include two different X-ray sources the values of f_X throughout this paper indicate the total, where each population gets a normalization factor equal to half the total.

Existing measurements can be used to constrain the value of f_X for each type of source. Fialkov et al. (2017) found that the unresolved soft X-ray background gives an upper limit for f_X that varies between $\sim$10 and 190 depending on the nature of the X-ray sources, the halo cooling channel and the value of the total CMB optical depth. A lower limit on f_X comes from measured upper limits on the 21-cm power spectrum (Ali et al. 2015) (which will be discussed below); Fialkov et al. (2017) found limits in the range of 0–0.036 (i.e. with some models unconstrained). In this paper, we take $f_X = 1$ as our standard value and mainly explore values in the range of 0.1–10, but consider also the extreme lower and upper limits from Fialkov et al. (2017).

3.3 CMB optical depth and mean free path of ionizing photons

The intensity of the 21-cm signal is proportional to the fraction of neutral hydrogen atoms in the IGM (equation 1), which is determined by the progress of cosmic reionization. According to current understanding, reionization happens inside out, proceeding first in the dense regions containing most of the sources (Barkana & Loeb 2004; Furlanetto, Zaldarriaga & Hernquist 2004; Iliev et al. 2006). The amplitude of the global 21-cm signal decreases as reionization advances.

A parameter that measures the total column density of ionized gas is the total CMB optical depth, τ. The latest and most precise constraints on τ come from the *Planck* satellite (Planck Collaboration et al. 2016a,b,c). However, the error in τ is still fairly large; moreover, the measured value of τ has gone down over time, and low values of τ are harder to measure since their imprint on the CMB is weaker. In particular, data analysis in 2015 (when we started our work) found an optical depth of $\tau = 0.066 \pm 0.016$ (Planck Collaboration et al. 2016a), which was smaller than previously measured; 2016 data gave $\tau = 0.055 \pm 0.009$ (Planck Collaboration et al. 2016c), while in a companion paper (Planck Collaboration et al. 2016b), which used a more realistic reionization model, a slightly higher value and uncertainty were reported, $\tau = 0.058 \pm 0.012$. Keeping in mind that in this work our main concern is to explore the widest parameter space possible, we adopt $\tau = 0.066$ as our standard value (it is difficult for us to produce much lower τ than this and still complete reionization by $z \sim 6$), and also consider $\tau = 0.082$ and $\tau = 0.098$, which are 1σ and $2\,\sigma$ away from the value reported by Planck Collaboration et al. (2016a). Because $\tau > 0.09$ is unlikely in the light of the latest results (i.e. it is ruled out at about the 3σ level), in the next section we mark all cases with $\tau > 0.09$ differently in the figures and we excluded these models from the fitting formulae.

The course of reionization depends also on the mean free path of ionizing photons. In particular, propagation of ionizing photons within the ionized regions is affected by the presence of absorption systems (Lyman-limit systems). We followed others (e.g. Greig & Mesinger 2015) in modelling this effect by imposing an upper limit on the mean free path of ionizing photons inside ionized regions, $R_{\rm mfp}$. We used the default value of $R_{\rm mfp} = 70$ Mpc (comoving) for most of the cases [this represents the maximum value expected and perhaps observed near the end of reionization (Wyithe & Loeb 2004)] but considered also the values of 20 and 5 Mpc.

3.4 The parameter space

In this section, we define the space of the discussed astrophysical parameters with the aim to (i) probe the range of possibilities for the global 21-cm signal and (ii) reasonably fill up the space within these boundaries. We stress that in this work we do not try to define the probability of each parameter set because the high-redshift universe is so poorly constrained. Before the 21-cm signal is detected, it is important to stay open-minded and allow for any reasonable realization within the allowed range.

We chose one model as a reference and refer to it as our 'standard' case. For this case, we used the atomic cooling scenario with $f_* = 0.05, f_X = 1$, XRBs as the (hard) X-ray sources and $\tau = 0.066$. Next, we considered small and large variations in the values of astrophysical parameters around the reference set by varying each parameter and considering all possible combinations. For the small variations (32 different parameter sets), we used either molecular cooling or massive haloes with f_* and f_X either larger or smaller by a factor of $\sqrt{10}$ from their standard values, our X-ray sources were either a mixture of XRBs and mini-quasars or a mixture of a soft SED and mini-quasars, and we assumed either $\tau = 0.066$ or $\tau = 0.082$. For the large variations, we took either metal cooling or supermassive haloes with f_* and f_X either larger or smaller by a factor of 10 from their standard values, either X-ray sources with a soft SED or mini-quasars, and either $\tau = 0.066$ or 0.098. This gave us 20 additional models (since others were ruled out by the above observations or the inability to achieve the desired τ). In terms of the X-ray sources, we note that mini-quasars give the case that is most different from a soft SED, since mini-quasars not only have a hard X-ray spectrum (which leads to weak early heating) but also decline faster with redshift (which weakens early heating even more). Thus, the SED cases in the 'small variations' category were roughly chosen to be intermediate compared to the 'large variations' and the 'standard case'. In addition, in order to fill up the global signal space with more intermediate models, we used all the combinations of the following parameters: $\tau = [0.066, 0.082]$, $f_* = [0.005, 0.05, 0.5]$, $f_X = [0.1, 1, 8]$, $V_c = [4.2, 16.5, 35.5]\,{\rm km\,s^{-1}}$ and SED = [soft, hard], which yielded 106 additional 'Space filler' parameter sets. Here, the high f_X value was chosen to be 8 rather than 10 in order to allow us to normalize all the models to τ as low as 6.6 per cent. For all the cases described above, we used $R_{\rm mfp} = 70$ Mpc. In addition, we considered some of the extreme cases with $R_{\rm mfp} = 20$ and 5 Mpc, in order to widen the total parameter space.

To obtain the desired optical depth in each case, we set the requisite value of the ionizing efficiency (Barkana & Loeb 2001; Furlanetto et al. 2006):

$$\zeta = f_* f_{\rm esc} N_{\rm ion} \frac{1}{1 + \bar{n}_{\rm rec}}, \tag{7}$$

where $f_{\rm esc}$ is the fraction of ionizing photons that escape into the IGM, $N_{\rm ion}$ is the mean number of ionizing photons produced per stellar baryon and $\bar{n}_{\rm rec}$ is the mean number of recombinations per ionized hydrogen atom. For each set of parameters, we tune ζ to produce the required optical depth while requiring the ionization fraction to be at least 95 per cent at $z = 6$. An upper limit on this parameter is $\zeta_{\rm max} = 40\,000 f_*$, where we use the value of $N_{\rm ion} = 40\,000$ for massive Population III stars (Bromm, Kudritzki & Loeb 2001). (We note that our models are based on numerical values for Population II stars, but by varying f_* and ζ we effectively cover a wide range of possibilities including the case of massive Population III stars.)

Some of our initial models were in conflict with recent upper limits on the 21-cm power spectrum reported by the PAPER collaboration (Ali et al. 2015). These data rule out models in which the 21-cm fluctuations at $z = 8.4$ are larger than 22 mK in the range of wavenumbers $k = 0.15$–$0.5\,h$ Mpc^{-1}, where h is the Hubble constant in units of 100 km s^{-1} Mpc^{-1}. Note that using this result to constrain the global signal directly is very model dependent [Pober et al. (2015) applied it for a specific model]. To make use of this constraint, we calculated the power spectrum for each case separately. Applying the optical depth normalization and the constraints from the PAPER experiment on our parameter space resulted in some large variation cases that had to be modified or excluded, leaving us with 20 such models.

In order to better explore the boundaries of the parameter space, we also added 22 different cases presented in Fialkov et al. (2017) (those not ruled out by the PAPER upper limits). In that paper the optical depth was not a free parameter but was instead determined by the redshift at which reionization ends (either late reionization with $z_{\rm re} = 6.2$ or early reionization with $z_{\rm re} = 8.5$). The scenarios of atomic and massive cooling with $f_* = 0.05$ were considered separately for each of the three types of X-ray sources (XRBs; mini-quasars and soft power law), while three different values were assigned for f_X — the upper limit defined by the unresolved soft X-ray background, the standard value of $f_X = 1$ and the lower limit defined by the PAPER constraint that applies only in the case of late reionization, while for the early reionization scenario, the lower limit on X-ray efficiency was $f_X = 0$. A summary of the parameter space is presented in Table 1, and the full list of cases is presented in the Appendix.

4 RESULTS

The parameter sets laid out in the previous section yield 193 total cases of the global 21-cm signal shown in Fig. 1, where the black line corresponds to the standard case with its three key turning points highlighted in red. This figure demonstrates how the large uncertainty in the astrophysical parameters introduced in Section 3 translates into a range of possibilities for the expected global 21-cm signal. The signal is sensitive to each of the variable astrophysical parameters and, thus, will have the power to constrain high-redshift astrophysics once it is detected.

Fig. 1 yields the first important conclusion of our parameter study: All the curves have the same basic qualitative shape as our standard case. The quantitative positions (in ν and $T_{\rm b}$) of the various key points vary amongst the curves, but the overall structure is fixed. We can intuitively understand this as follows. The low optical depth from *Planck* basically fixes reionization to occur at the low end of the redshift range we cover, with reionization completing at $z \sim 6$–9. At the other end, the Ly$\,\alpha$ intensity required to produce Ly$\,\alpha$ coupling is rather low, so that stars (assuming they contribute significantly to reionization) naturally saturate Ly$\,\alpha$ coupling long before a significant fraction of the Universe is reionized. As for X-ray heating, it can occur at a wide range of redshifts, much earlier than reionization in the case of strong heating with a soft SED and low optical depth, or as late as the very end of reionization for scenarios with hard X-ray sources and reionization at the high end of the optical depth range consistent with *Planck* data (Fialkov et al. 2014; Fialkov & Barkana 2014; Fialkov & Loeb 2016; Madau & Fragos 2017; Mirocha et al. 2017). Importantly, though, X-ray heating always begins somewhat *after* the beginning of significant Ly$\,\alpha$ coupling. Our results are thus reassuring, but they do not imply that models that violate this basic shape are completely ruled out, though such models do appear highly unlikely. For example, extremely strong X-ray heating could occur prior to Ly$\,\alpha$ coupling (i.e. at $z \sim 30$) and prevent an absorption minimum, but in order for such an intense X-ray outburst to avoid overproducing the observed X-ray background, the associated source population would have to essentially disappear by $z \sim 10$ (Fialkov et al. 2017) despite the rapid ramp-up of galaxy formation. We also note that a different version of Fig. 1 is shown later, at the end of this section.

In this section, we use our 193 different cases to explore the correlation between the features of the global 21-cm signal and physical properties of the high-redshift universe, showing that the neutral hydrogen signal alone has enough predictive power to constrain some details of primordial star formation, heating and reionization as well as the typical halo mass. We analyse the properties of the 21-cm signal starting from high redshifts at which the Universe was cold and empty (and thus easy to analyse), then continuing to lower redshifts at which various astrophysical processes caused non-local feedback effects on star formation, complicating the picture.

4.1 High-z maximum point

As noted in Section 2, the high-redshift maximum of the global 21-cm curve is the point at which the first population of Ly$\,\alpha$ sources (assumed to be stars) turns on, and the Wouthuysen-Field coupling starts to become effective. At this point, the Universe is still relatively simple, as stars are rare and have not yet had a significant effect on the 21-cm intensity. The only parameters that have an effect on the 21-cm signal at this point are the minimum mass of star-forming haloes and the star formation efficiency, which together determine the Ly$\,\alpha$ intensity and thus the strength of the Ly$\,\alpha$ coupling. The parameters related to heating and reionization are not yet important. In the absence of collisions and Ly$\,\alpha$ photons, interactions with the CMB would drive T_S to $T_{\rm CMB}$ and thus the differential brightness temperature would be zero. At $z \sim 35$, collisions, which had kept T_s close to $T_{\rm gas}$ at higher redshift, become less and less effective with time, so that $T_{\rm b}$ (which is negative) rises towards zero. This portion of the global 21-cm curve is still within the 'dark ages', i.e. precisely predictable given the basic cosmological parameters.

The high-redshift maximum is produced just as the first significant Ly$\,\alpha$ coupling causes $T_{\rm b}$ to start becoming more negative. Thus, the high-z maximum occurs near the dark ages curve, so we expect to see an approximate relation between the redshift of the maximal point, $z^{\rm hi}_{\rm max}$, and the value of the brightness temperature at this point, $T^{\rm hi}_{\rm b,max}$; specifically the lower the $z^{\rm hi}_{\rm max}$, the closer $T^{\rm hi}_{\rm b,max}$ should be to zero. We indeed observe a rather clear relation in our models, as shown in Fig. 2. We find the following approximate fitting formula:

$$T^{\rm hi}_{\rm b,max} = a\left(1+z^{\rm hi}_{\rm max}\right)^2 + b\left(1+z^{\rm hi}_{\rm max}\right) + c, \quad (8)$$

where $[a, b, c] = [-0.03124, 1.155, -10.65]$ (We note that Mirocha et al. (2013) used an analytical analysis for an approximate study of this dependence). At the highest redshifts, the dark ages global 21-cm curve rises steeply, so that it takes some time for it to turn over due to Ly$\,\alpha$ radiation, and the maximum point occurs below the dark ages curve by $\sim$2 mK at a given redshift; at lower redshifts, the dark ages curve is flatter so that the maximum occurs almost immediately once the actual curve deviates from the dark ages limit.

Since the relation between $T^{\rm hi}_{\rm b,max}$ and $z^{\rm hi}_{\rm max}$ is monotonic and there is almost no scatter, it would suffice to measure either the brightness temperature or the redshift to obtain all the information on this extremum of the global signal (though measuring both would provide a clear consistency test and verification that the expected signal is indeed being observed). From this measurement, it should

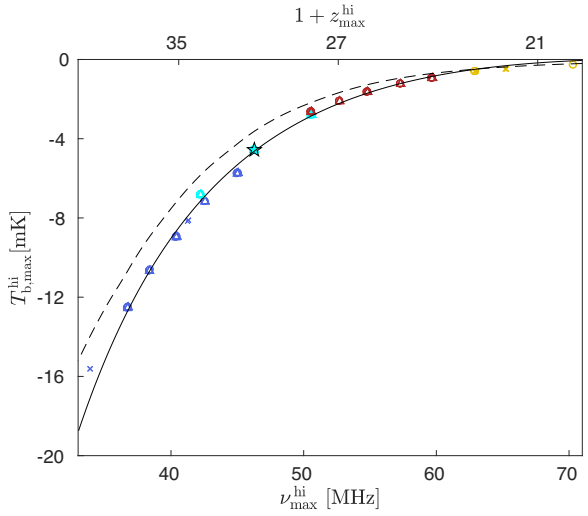

Figure 2. Brightness temperature as a function of observed frequency (bottom axis) or the equivalent one plus redshift (top axis) at the high-z maximum point. The colours indicate the minimum circular velocity of star-forming haloes for each case: $V_c = 4.2$ (blue), 16.5 (cyan), 35.5 (red) and 76.5 km s^{-1} (yellow). Shapes indicate the optical depth for each case: $\tau = 0.060$–0.075 (circles), 0.082–0.09 (triangles), 0.09–0.111 (crosses), while the star is our standard case. Also shown are the fitting function of equation (8) (solid curve) and the dark ages (i.e. no astrophysical radiation) relation (dashed curve).

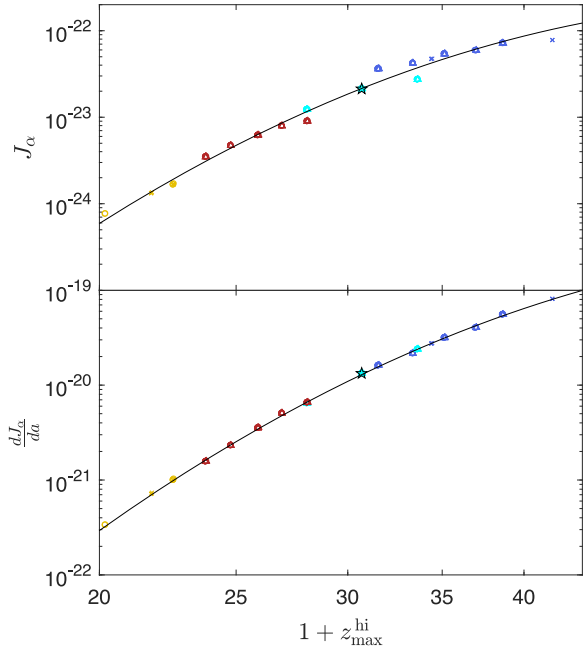

Figure 3. The Ly α intensity (top panel) in units of erg s^{-1} cm^{-2} Hz^{-1} sr^{-1} and its derivative with respect to the scale factor (bottom panel) as a function of $z^{\rm hi}_{\rm max}$. The colour indicates the cooling channel for each case: $V_c = 4.2$ (blue), 16.5 (cyan), 35.5 (red), 76.5 km s^{-1} (yellow). Shapes indicate the optical depth for each case: $\tau = 0.060$–0.075 (circles), 0.082–0.09 (triangles), 0.09–0.111 (crosses), while the star is our standard case. Also shown (black lines) are the fitting function equation (9) (top panel) and equation (10) (bottom panel).

be possible to roughly estimate the value of the minimum V_c (shown by different colours in the figure), with an uncertainty introduced by the possible range of the SFE. As expected, smaller V_c implies earlier the star formation and thus a more negative value of $T^{\rm hi}_{\rm b,max}$.

In addition to considering predicted relations amongst observables of the global 21-cm spectrum, our other goal in this paper is to explore whether astrophysical information can be easily extracted. Additional information that could be extracted the high-z maximum were measured is the average intensity of the Ly α background at this epoch, i.e. at redshift $z^{\rm hi}_{\rm max}$. As can be seen from Fig. 3, the observables can be used to accurately reconstruct the angle-averaged intensity of Ly α photons, J_α, as well as its derivative with respect to the scale factor, a [both spatially-averaged over the universe). This is true whether we use the redshift, as shown, or the brightness temperature (which is strongly correlated with it based on Fig. 2)].

We fit the dependence with the following functions (hereafter, log means base 10):

$$\log\left(J_\alpha\right) = a_1 \log^2\left(1+z^{\rm hi}_{\rm max}\right) + b_1 \log\left(1+z^{\rm hi}_{\rm max}\right) + c_1, \quad (9)$$

$$\log\left(\frac{{\rm d}J_\alpha}{{\rm d}a}\right) = a_2 \log^2\left(1+z^{\rm hi}_{\rm max}\right) + b_2 \log\left(1+z^{\rm hi}_{\rm max}\right) + c_2, \quad (10)$$

where $[a_1,\ b_1,\ c_1] = [-10.39,\ 37.36,\ -55.247]$ and $[a_2,\ b_2,\ c_2] = [-9.238,\ 34.59,\ -50.897]$, and J_α is in units of erg s^{-1} cm^{-2} Hz^{-1} sr^{-1}. Fig. 3 shows that the scatter in these relations is fairly small, especially for the derivative of the intensity, since the rapid change in time in J_α makes the extremum condition especially sensitive to the derivative. If the time derivative of the Lyα intensity is determined in this way, this would provide information on a combination of the minimum halo V_c and the star formation efficiency.

4.2 Minimum point

The next prominent feature of the global 21-cm signal is the absorption trough, with the minimum defined by the beginning of the heating era in combination with Ly α saturation. The location of this point depends on more parameters (the X-ray efficiency and SED in addition to V_c and f_*), which leads to a larger scatter of possible values of the minimal brightness temperature $T_{\rm b,min}$ and the redshift at which it is achieved $z_{\rm min}$. While for our standard case the minimum point occurs at $z_{\rm min} = 18$ with a depth of $T_{\rm b,\,min} = -170$ mK, variation of the astrophysical parameters leads to a range in redshift $10.9 < z_{\rm min} < 26.5$ and temperatures -240 mK $< T_{\rm b,\,min} < -25$ mK. As can be seen in Fig. 4, there is no predicted relation between these two observables, the redshift and the temperature, e.g. for any given redshift of the minimum a large range of corresponding temperatures is possible.

We can understand how some of the parameters produce the large scatter in the plot. Points with the same f_* (marked by the same colour in Fig. 4) are roughly aligned along diagonal lines going from the top left to the bottom right of the plot. Different lines of the same colour correspond to different values of V_c, while the scattering of points along a given line is due to variations in the intensity and SED of the X-ray radiation. Lower values of V_c lead to higher $z_{\rm min}$, while a lower X-ray heating rate results in a more negative value of $T_{\rm b,\,min}$.

A lower limit on the brightness temperature can be obtained assuming a fully neutral universe with no X-ray sources (i.e. where the gas cools adiabatically after thermal decoupling from the CMB)

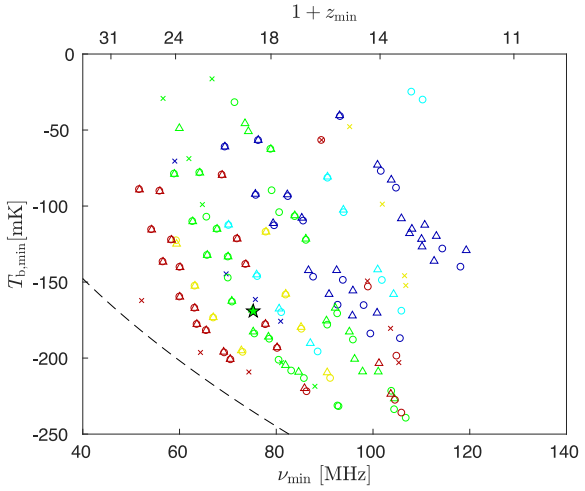

Figure 4. Brightness temperature at the minimum point as a function of observed frequency of this point (bottom axis) or the equivalent one plus redshift (top axis). The colours indicate the star formation efficiency for each case: $f_* = 0.005$ (blue), 0.016 (cyan), 0.05 (green), 0.16 (yellow), 0.5 (red). Also shown (black dashed line) is the lower limit on the brightness temperature at each redshift from the no-heating limit (equation 11). Shapes indicate the optical depth for each case: $\tau = 0.060$–0.075 (circles), 0.082–0.09 (triangles), 0.09–0.111 (crosses), while the star is our standard case.

but full Ly α coupling (i.e. $T_S = T_{\rm gas}$). In this limit, using equation (1) we can derive the following relation for the mean temperature:

$$T_{\rm b,min} \geq 26.8 \left(\frac{1+z_{\rm min}}{10}\right)^{1/2} \left(1 - \frac{1+z_{\rm dec}}{1+z_{\rm min}}\right) {\rm mK}, \quad (11)$$

where $z_{\rm dec} = 137$ is the redshift at which the gas temperature and the CMB temperature effectively decoupled. Following the same logic, we can write

$$1 - \frac{T_{\rm b,min}}{26.8\sqrt{\frac{1+z_{\rm min}}{10}}} \leq \frac{T_{\rm CMB}}{T_{\rm gas}} \leq \frac{1+z_{\rm dec}}{1+z_{\rm min}} \, . \quad (12)$$

Fig. 5 shows the ratio $T_{\rm CMB}/T_{\rm gas}$ as a function of the brightness temperature or the redshift at the minimum point. The black dashed line in the left-hand panel shows the left-hand side of equation (12) calculated at $z_{\rm min} = 18$ that corresponds to $z_{\rm min}$ in our standard case. Since the redshift dependence is weak, taking a constant redshift is a good approximation to the case where the spin temperature is fully coupled to the gas temperature (note also that the reionized fraction is quite low at this stage in our models). While many of our simulated models lie close to this line, implying that they have nearly achieved saturated Ly α coupling, a substantial fraction is well away from the line, showing that for them the Wouthuysen–Field coupling is still far from saturation. The strength of the coupling is determined by the Ly α intensity and is stronger for models with large f_* and small V_c. The black dashed line in the right-hand panel of Fig. 5 shows the right-hand side of equation (12). Here too, while many models show little heating (i.e. are close to the line), a substantial fraction has undergone significant heating prior to reaching the minimum. Even when heating begins, in order to produce a global 21-cm minimum it must overcome two effects: adiabatic cooling (astrophysical heating initially only slows down the rate of cooling) and the increase with time of the Ly α coupling (which, as long as it is not yet saturated, pushes $T_{\rm b}$ to be more negative). The two panels of Fig. 5 together show the large variety of physical conditions that leads to the large scatter in the position of the minimum point.

Despite the complexity, we have managed to find some order in the relation between the properties of the minimum and the underlying astrophysical properties of interest. Specifically, the depth of the minimum point is strongly correlated with the ratio between the average Ly α intensity and the X-ray heating rate, as shown in Fig. 6. The correlation is easy to explain: with a large X-ray heating rate, heating starts earlier and the brightness temperature at the minimum (the redshift of which depends also on Ly α saturation) is less negative. On the other hand, large Ly α intensity leads to stronger coupling between the spin temperature and the gas temperature, and, thus, to a more negative brightness temperature when significant heating begins and produces the minimum. We also show in

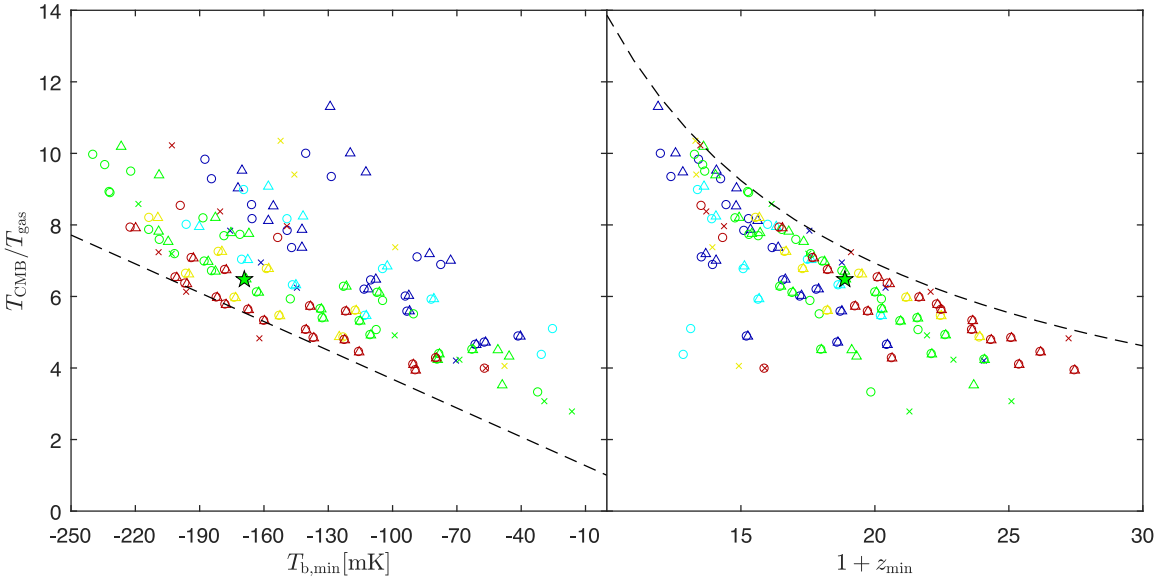

Figure 5. The ratio $T_{\rm CMB}/T_{\rm gas}$ as a function of the brightness temperature (left-hand panel) and of the redshift (right-hand panel) at the minimum point. The colours indicate the star formation efficiency for each case: $f_* = 0.005$ (blue), 0.016 (cyan), 0.05 (green), 0.16 (yellow), 0.5 (red). Shapes indicate the optical depth for each case: $\tau = 0.060$–0.075 (circles), 0.082–0.09 (triangles), 0.09–0.111 (crosses), while the star is our standard case. Also shown (dashed black lines) is the lower limit on $T_{\rm CMB}/T_{\rm gas}$ (left-hand panel) and upper limit on $T_{\rm CMB}/T_{\rm gas}$ (right-hand panel); see equation (12) and the text for details.

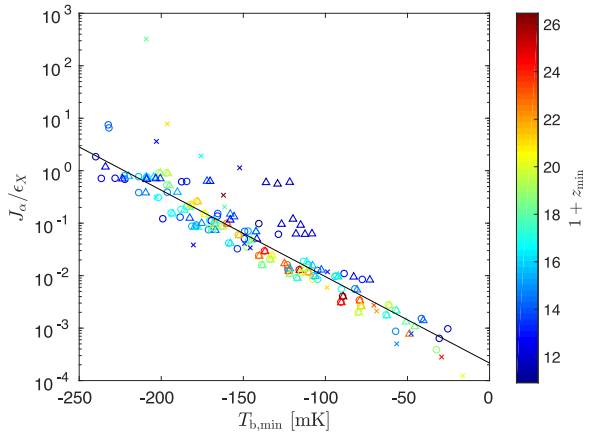

Figure 6. The ratio between the Lyα intensity (in units of erg s^{-1} cm^{-2} Hz^{-1} sr^{-1}) and the X-ray heating rate (in units of eV s^{-1} baryon^{-1}) as a function of the brightness temperature at the minimum point. The colour indicates the redshift of the minimum point (see the colour bar on the right). Also shown is the fitting function of equation (13) (black line). Shapes indicate the optical depth for each case: $\tau = 0.060$–0.075 (circles), 0.082–0.09 (triangles), 0.09–0.111 (crosses), while the star is our standard case. Note that the point with the largest ratio represents an extreme case in which X-ray sources are mini-quasars and $f_X = 0.1$, which means an extremely low X-ray heating rate at this redshift, while metal cooling with $f_* = 0.5$ drives up J_α.

Fig. 6 a fitting function (always excluding $\tau > 0.09$ cases, as noted previously):

$$\log\left(\frac{J_\alpha}{\epsilon_X}\right) = aT_{\rm b,min} + b, \tag{13}$$

with $[a, b] = [-0.016, -3.666]$, where ϵ_X is the heating rate in units of eV s^{-1} per baryon in the IGM. Thus, measuring the minimum point, which is expected to be the most prominent feature of the global 21-cm signal, will provide us a fairly good estimate of J_α/ϵ_X at the corresponding redshift.

4.3 Low-z maximum point

The lowest-redshift extremum in the global 21-cm curve is the low-z maximum. In models where X-ray sources are efficient and heat the gas well above the temperature of the CMB early enough, the 21-cm signal is seen in emission during the later stages of cosmic evolution. Heating increases the emission signal until heating saturates ($T_{\rm gas} \gg T_{\rm CMB}$), producing another maximum in the global 21-cm signal, of height $T^{\rm lo}_{\rm b,max}$ and redshift $z^{\rm lo}_{\rm max}$. The position of the maximum is also affected by the advance of reionization. As more and more stars appear and galaxies grow, the bubbles of reionized gas expand. Reionization suppresses the neutral fraction and thus the intensity of the signal, helping produce the maximum earlier while decreasing its brightness temperature. In some models, including the currently most likely heating cases (Fialkov et al. 2014; Fialkov & Loeb 2016; Fialkov et al. 2017; Mirocha et al. 2017; Madau & Fragos 2017), heating is not saturated by the beginning of reionization, the 21-cm signal is driven by heating and reionization simultaneously, and the emission feature is not so prominent. Furthermore, in cases of extremely low heating the gas in neutral regions is colder than the CMB even at the end of reionization (Fialkov & Loeb 2016; Fialkov et al. 2017) and should be seen in absorption against the CMB at all redshifts, with no emission peak. In these cases, where there is no low-z maximum, we set $T^{\rm lo}_{\rm b,max}$ to zero and $z^{\rm lo}_{\rm max}$ to the end of reionization.

The left-hand panel of Fig. 7 shows the scatter of the low-redshift maximum point for all the considered models in the $T^{\rm lo}_{\rm b,max}$ versus ν (or $z^{\rm lo}_{\rm max}$) plane. The emission signal cannot be stronger than the upper limit obtained for a fully neutral universe ($x_{\rm H\,I} = 1$) and saturated heating:

$$T^{\rm lo}_{\rm b,max} = 26.8\left(\frac{1+z^{\rm lo}_{\rm max}}{10}\right)^{1/2}\ {\rm mK}. \tag{14}$$

Usually heating is near saturation at the low-z max, and the distance between the model points in Fig. 7 and the dashed line (equation 14) mostly expresses the advance of reionization towards low redshift. Current CMB observations restrict our models to a fairly narrow range of reionization histories, particularly if we restrict the optical depth to values consistent with current measurements to within 2σ (roughly the blue points in the figure). Moreover, the dependence on optical depth is easy to explain: in cases with lower optical depth reionization starts later and thus, at a given $z^{\rm lo}_{\rm max}$, it is less well advanced, and the emission signal $T^{\rm lo}_{\rm b,max}$ is higher.

In general, models with strong heating tend to produce an emission signal, and then saturated heating, at higher redshifts, already at an early stage of reionization. In these cases, the neutral fraction is still high, and the value of $T^{\rm lo}_{\rm b,max}$ is closer to the upper limit defined by equation (14). Extreme models with the strongest X-ray emission feature a significant X-ray contribution to reionization, which helps keep the high-redshift data points away from the dashed line in Fig. 7. On the other hand, models with weak heating need more time to arrive at the saturation point, and thus the peak of the emission signal happens during advanced stages of reionization by stellar sources ($x_{\rm H\,I} \ll 1$). Thus, the amplitude of the emission maximum is much lower than the upper bound and $z^{\rm lo}_{\rm max}$ is then closer to the end of reionization. When considering the full ensemble of models, a roughly linear dependence between the temperature and the frequency can be seen (excluding the $T^{\rm lo}_{\rm b,max} = 0$ points; left-hand panel of Fig. 7), which is well fitted by

$$T^{\rm lo}_{\rm b,max} = \begin{cases} a\frac{1}{1+z^{\rm lo}_{\rm max}} + b, & \text{if } 1+z^{\rm lo}_{\rm max} > \frac{-a}{b}, \\ 0, & \text{otherwise,} \end{cases} \tag{15}$$

where $[a, b] = [-562.8, 63.9]$.

We have found some interesting trends related to the low-redshift emission point. Specifically, the strength of the emission signal can be related to some of the astrophysical parameters at that epoch, thus directly constraining heating sources and star formation. We find that the intensity of the emission signal is correlated with the heating rate at $z^{\rm lo}_{\rm max}$ (Fig. 7, right-hand panel), with the relation well fitted by

$$\log(\epsilon_X) = aT^{\rm lo}_{\rm b,max} + b, \tag{16}$$

where $[a, b] = [0.080, -18.2]$. The qualitative dependence is easy to explain following the same lines as above: the larger the heating rate, the earlier X-ray heating saturates and the stronger is the emission feature in the absence of much reionization by UV sources. Another striking correlation involves also the production of ionizing photons. We use $\zeta f_{\rm coll}$ as a measure for the produced amount of ionizing photons, where $f_{\rm coll}$ is the fraction of mass in star-forming haloes (often called the 'collapsed fraction'), which depends on V_c, and ζ is the overall ionizing efficiency (equation 7). We plot the ratio of heating rate to ionization production ($\epsilon_X/[\zeta f_{\rm coll}]$) as a function of peak brightness temperature $T^{\rm lo}_{\rm b,max}$ (Fig. 8). Along the same lines of reasoning as above, it is clear that to get large values of $T^{\rm lo}_{\rm max}$ a

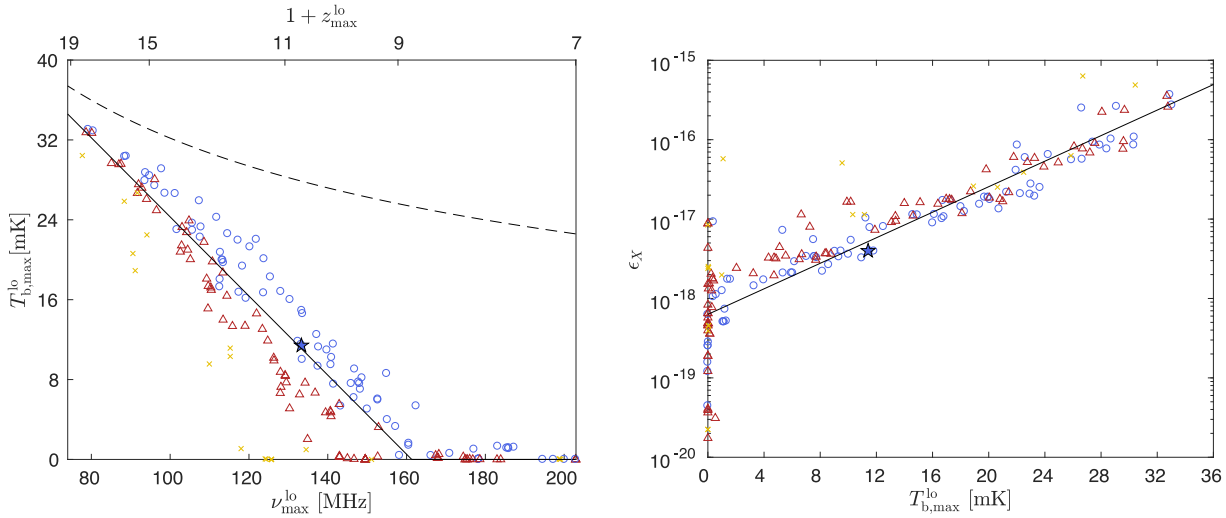

Figure 7. Left panel: Brightness temperature as a function of observed frequency (bottom axis) or equivalent one plus redshift (top axis) at the low-z maximum point. Also shown is the fitting function given by equation (15) (black solid line) and the upper limit from equation (14) (black dashed line). Right panel: The X-ray heating rate (in units of eV s^{-1} baryon^{-1}) as a function of the brightness temperature at the low-z maximum. Also shown is the fitting function from equation (16) (black line). In both panels the colours indicate the optical depth for each case: $\tau = 0.060$–0.075 (blue), 0.082–0.09 (brown), 0.09–0.111 (yellow crosses); the star is our standard case.

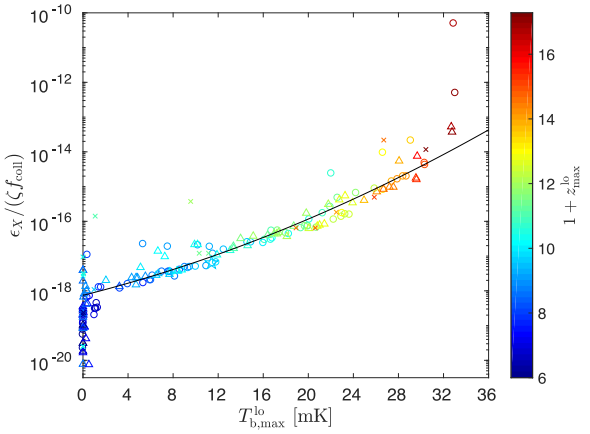

Figure 8. The ratio between the heating rate of X-ray sources, ϵ_X (in units of eV s^{-1} baryon^{-1}), and the production of ionizing photons as measured by $\zeta f_{\rm coll}$, as a function of the brightness temperature at the low-z maximum point. The colour (see the colour bar on the right) indicates the corresponding redshift of the low-z maximum point. Also shown is the fitting function of equation (17) (solid black line). Shapes indicate the optical depth for each case: $\tau = 0.060$–0.075 (circles), 0.082–0.09 (triangles), 0.09–0.111 (crosses), while the star is our standard case.

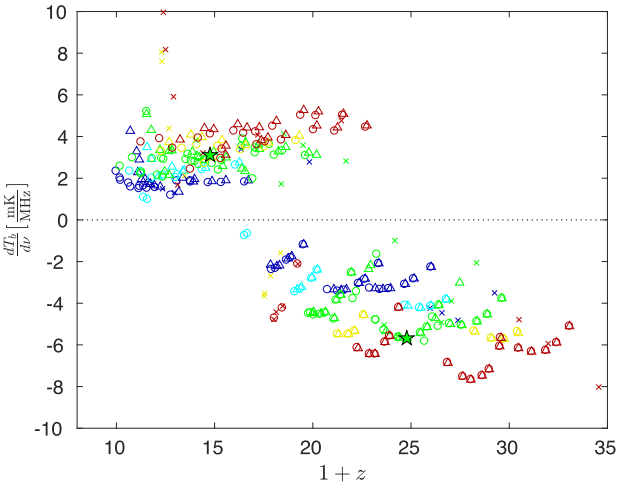

Figure 9. The mean slope of $T_{\rm b}$ versus ν between $z^{\rm hi}_{\rm max}$ and $z_{\rm min}$ (the negative slope) as a function of $1+(z_{\rm min}+z^{\rm hi}_{\rm max})/2$, and the mean slope between $z_{\rm min}$ and $z^{\rm lo}_{\rm max}$ (the positive slope) as a function of $1+(z_{\rm min}+z^{\rm lo}_{\rm max})/!2$. Colours indicate different values of the star formation efficiency: $f_* = 0.005$ (blue), 0.016 (cyan), 0.05 (green), 0.16 (yellow), 0.5 (red). Shapes indicate the optical depth for each case: $\tau = 0.060$–0.075 (circles), 0.082–0.09 (triangles), 0.09–0.111 (crosses), while the star is our standard case.

strong heating (which gives an early peak) together with weak ionization (which keeps the neutral hydrogen fraction high) is required. This relation can be fitted by

$$\log\left(\frac{\epsilon_X}{\zeta\, f_{\rm coll}}\right) = a\left[T^{\rm lo}_{\rm b,max}\right]^2 + bT^{\rm lo}_{\rm b,max} + c, \qquad (17)$$

where $[a, b] = [0.0014, 0.082, -18.13]$, and we excluded from the fit points with $T^{\rm lo}_{\rm b,max} = 0$ or $T^{\rm lo}_{\rm b,max} > 32$ mK (or, as always, $\tau > .09$). Because the relation between $T^{\rm lo}_{\rm b,max}$ and $z^{\rm lo}_{\rm max}$ is largely monotonic as follows from equation (15) and is also indicated by the colour map in Fig. 8, it is also possible to express the ratio as a function of $z^{\rm lo}_{\rm max}$ instead of the peak brightness temperature. E and (17) should enable us to estimate the X-ray heating rate and $\zeta f_{\rm coll}$ at $z^{\rm lo}_{\rm max}$ from future measurements of the global 21-cm signal.

4.4 Average slopes

In addition to the three key points discussed above, the derivative (slope) of the signal with respect to frequency is interesting to consider separately, because it is likely easier to measure than the absolute signal itself due to the need for foreground removal. We use the key inflection points to define two characteristic slopes, for each model: the mean slope between the high-z maximum point and the minimum point (a negative slope), and the mean slope between the minimum point and the low-z maximum point (a positive slope). This allows us to visualize a kind of summary of the entire relevant range of the global 21-cm curve, by plotting both the positive and negative slopes together in Fig. 9. Each slope is shown as a function

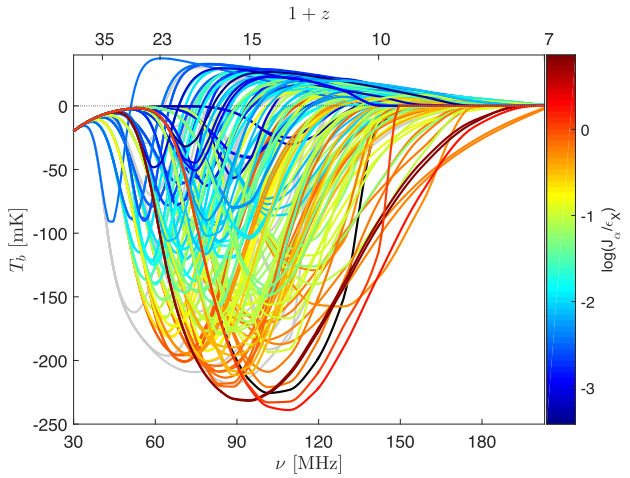

Figure 10. The 21-cm global signal as a function of redshift, for our 193 different astrophysical models, as in Fig. 1. The colour (see the colour bar on the right) indicates the ratio between the Ly α intensity (in units of erg s^{-1} cm^{-2} Hz^{-1} sr^{-1}) and the X-ray heating rate (in units of eV s^{-1} $baryon^{-1}$) at the minimum point. Grey curves indicate cases with $\tau > 0.09$, and a non-excluded $f_X = 0$ case is in black; these cases are all excluded from the colour bar range.

of the mean one plus redshift at which it is measured, i.e. $1 + \left(z_{\rm min} + z^{\rm hi}_{\rm max}\right)/2$ for the negative slope and $1 + \left(z_{\rm min} + z^{\rm lo}_{\rm max}\right)/!2$ for the positive slope.

Because each slope depends on the intensity and redshift of the global signal at two of the turning points, the dependence on our various parameters is more complex, and it is difficult to extract simple relations between the slopes and astrophysical quantities. One general trend is that a high star formation efficiency tends to produce strong radiation fields early on, thus high redshifts for the key points that imply shorter frequency intervals, resulting in steep slopes (both positive and negative). The overall range of slopes is roughly -1 to -8 mK/MHz (negative) and 1–5 mK/MHz (positive), with the negative slope typically nearly twice the positive one (in absolute value). Of course, the foreground emission is also substantially larger at the higher redshift range corresponding to the negative slope. Note that a very large positive slope ($dT_b/d\nu \gtrsim 6$ mK/MHz) can only be produced by having reionization so early that the resulting optical depth is excluded by *Planck* at 3σ.

4.5 Summary plot

Given the various results shown thus far in this section, in particular the correlations between observable features and various astrophysical parameters, we can construct a plot that partly summarizes the correlations while showing the full global 21-cm curves. Fig. 10 is another version of Fig. 1, but with additional information that brings some order. First, cases with $\tau > 0.09$ are shown as grey. The remaining curves are colour coded according to the corresponding ratio in each model between the Ly α intensity and the X-ray heating rate at $z_{\rm min}$ (i.e. at the time of the minimum point of the global 21-cm curve). This is the same ratio plotted in Fig. 6) and shown there to correlate closely with the depth of the minimum, $T_{\rm b,\,min}$. While no single parameter can fully describe the global 21-cm curve, Fig. 10 does show that this particular ratio nicely slices up the parameter space of possible curves. Those with a high ratio tend to fill the bottom right portion of the figure, i.e. they usually produce a deep minimum and maintain a 21-cm absorption signal until fairly late; models with a low ratio, on the other hand, tend to fill the upper left, producing a shallow minimum and early 21-cm emission. Note that the colour coding also makes it easier to trace individual global 21-cm curves within this plot, in order to appreciate the variety of curves that are possible.

5 SUMMARY AND DISCUSSION

In this paper, we have explored the allowed parameter space of the global 21-cm signal, varying the main high-redshift astrophysical parameters such as the minimal mass of star-forming haloes, star formation efficiency, and heating and ionization rates, all of which are poorly constrained. The large uncertainty in high-redshift astrophysical processes results in weak limits on the predicted 21-cm signal. We used a realistic semi-numerical simulation to produce the 21-cm global signal in the redshift range of $z = 6$–40 for 193 different sets of astrophysical parameters in agreement with current observations (except that 21 are excluded by the *Planck* measurement of optical depth at $3\,\sigma$). We applied these data to establish universal patterns in the predicted global 21-cm curves. We found that the general shape of the signal can be predicted theoretically, but its features remain highly unconstrained. Still, there are clear correlations between the three key features of the global 21-cm signal (the high-z maximum, the minimum and the low-z maximum points) and underlying astrophysical parameters of the early universe. Our compilation of realistic models and fitting formulae for these correlations can be used to rule out portions of the parameter space as data from ongoing and future radio experiments becomes available. If and when the global signal is measured, our results can be used to reconstructed key aspects of the high-redshift population of sources including the first stars, XRBs and mini-quasars.

The parameters that we varied can be divided into three categories. The first group consists of parameters related to primordial star formation, including the minimum mass of haloes in which stars can form and the star formation efficiency. These parameters are the only ones that affect the shape of the global signal (through the Ly α intensity) from the formation of the first stars down to the redshift where X-ray sources turn on. The second group captures properties of the first heating sources, including their X-ray spectra, luminosity and evolution with redshift (e.g. XRBs versus mini-quasars), which together with the properties of star formation affect the shape of the signal from the moment when X-ray sources turn on to the point when reionization becomes significant. Finally, the CMB optical depth is related to ionization properties of stars that drive the global signal at the low-redshift end.

As anticipated, properties of the high-z maximum point are relatively simple because it occurs at high redshift where significant Ly α coupling begins, which in all our models occurs before heating and ionizing sources and complicate the evolution of the global signal. There is a close relation between the redshift of this turning point and the corresponding intensity of the 21-cm signal, providing a potential consistency check for observations. These observable quantities also correlate closely with the Ly α intensity and its derivative at that epoch, according to fitting formulae that we have obtained. Thus, measuring the global signal at this point would help determine the total star formation rate at this early epoch, thus constraining a combination of the minimum cooling mass of star-forming haloes and the star formation efficiency.

The redshift and depth of the absorption trough show the largest scatter, since this minimum can occur under various physical conditions and is affected by many astrophysical parameters. It typically

occurs when Lyα coupling approaches saturation and significant X-ray heating begins. In most models, the absorption trough is the strongest feature of the signal and its detection is one of the main goals of the global 21-cm experiments; the large predicted scatter in the location of this point should encourage observers to search for the signal in as wide a frequency range as possible. Measuring the redshift and depth of the absorption trough alone would not help us to strongly constrain any single parameter, but can be used to rule out some areas of the astrophysical parameter space. Despite this complexity, we have shown that the depth of the absorption trough of the 21-cm signal is strongly correlated with the ratio between the Lyα intensity and the X-ray heating rate, as given by a corresponding fitting formula.

The 21-cm signal from the low-z maximum is typically expected to be seen in emission, once heating approaches saturation (unless heating occurs very late). This maximum is affected by both cosmic heating and reionization, so in our models it is affected by both the total CMB optical depth and the properties of X-ray sources, with some scatter introduced by other parameters. For maxima that take place at late times the signal is weaker since reionization is then more advanced. We did fit simple functions to show relations between (1) the redshift and the brightness temperature of this point, (2) the heating rate and the brightness temperature and (3) the ratio of the heating rate to the ionization production and the brightness temperature. Therefore, measurement of the redshift and temperature at the emission peak would give a self-consistency check and allow us to estimate both the X-ray and ionizing intensity of sources.

Taken together, the correlations in equations (9), (10), (13), (16), and (17) can be used to directly link future measurements of the global 21-cm signal to astrophysical properties of the high redshift Universe, in a mostly model-independent way. Meanwhile, those in equations (8) and (15) can be used as consistency checks on the measurements (or on the theory, depending on one's point of view). Some caution is advisable, as models like ours do not capture the full possible complexity of high-redshift astrophysics. For example, f_* and the other efficiency parameters could vary with redshift, with the local density, or show a large scatter amongst haloes. We expect the main effect of this to be that the correlations that we identified at each key turning point will measure the astrophysical parameters as averaged spatially and over time (out to an earlier time than that corresponding to a given key feature). Also, the scatter could increase in some correlations, particularly those that depend on multiple redshifts as in Fig. 9. We plan to explore how more elaborate models affect our results. Some of our conclusions are reminiscent of those found by Mirocha et al. (2013), now derived in the context of a wider array of astrophysical models and more realistic simulations; a conclusion that is particularly similar is that the high-z maximum point reflects the Lyα intensity and its time derivative.

We have tried to cover as large a parameter space as possible, in terms of astrophysical source formation, radiative efficiencies, feedback effects and the mean free path of ionizing photons. The goal was to make our conclusions as robust as possible given current uncertainties about high-redshift astrophysics. However, in the results we have focused only on some of the parameters and a few correlations, namely those that were cleanest and thus most useful. We have explored many others that did not give a clearly useful result, and we plan to continue such studies.

Current and future 21-cm observations, such as those mentioned in the Introduction section, are expected to soon begin to exclude realistic possible realizations of the global 21-cm signal. We hope this is followed soon afterwards with detections, which will probe currently mysterious astrophysical processes at very high redshifts.

ACKNOWLEDGEMENTS

We thank Joe Lazio for a suggestion that led us to Fig. 10. RB, AC and ML acknowledge Israel Science Foundation grant 823/09 and the Ministry of Science and Technology, Israel. For RB and AC, this project/publication was made possible through the support of a grant from the John Templeton Foundation. The opinions expressed in this publication are those of the author(s) and do not necessarily reflect the views of the John Templeton Foundation. RB's work has been partly done within the Labex Institut Lagrange de Paris (ILP, reference ANR-10-LABX-63) part of the Idex SUPER, and received financial state aid managed by the Agence Nationale de la Recherche, as part of the programme Investissements d'avenir under the reference ANR-11-IDEX-0004-02. RB also acknowledges a Leverhulme Trust Visiting Professorship at the University of Oxford. This research was supported in part by Perimeter Institute for Theoretical Physics. Research at Perimeter Institute is supported by the Government of Canada through the Department of Innovation, Science and Economic Development Canada and by the Province of Ontario through the Ministry of Research, Innovation and Science.

REFERENCES

Ali Z. S. et al., 2015, ApJ, 809, 61
Barkana R., 2016, Phys. Rep., 645, 1
Barkana R., Loeb A., 2001, Phys. Rep., 349, 125
Barkana R., Loeb A., 2004, ApJ, 609, 474
Barkana R., Loeb A., 2005a, ApJ, 624, L65
Barkana R., Loeb A., 2005b, ApJ, 626, 1
Behroozi P. S., Silk J., 2015, ApJ, 799, 32
Bernardi G., McQuinn M., Greenhill L. J., 2015, ApJ, 799, 90
Bernardi G. et al., 2016, MNRAS, 461, 2847
Bharadwaj S., Ali S. S., 2004, MNRAS, 352, 142
Bowman J. D., Rogers A. E. E., 2010, Nature, 468, 796
Bowman J. D. et al., 2013, PASA, 30, 31
Bromm V., Kudritzki R. P., Loeb A., 2001, ApJ, 552, 464
Bromm V., Coppi P. S., Larson R. B., 2002, ApJ, 564, 23
Burns J. O., Lazio J., Bale S., Bowman J., Bradley R. et al., 2012, Adv. Space Res., 49, 433
Cirelli M., Iocco F., Panci P., 2009, JCAP, 10, 009
Cohen A., Fialkov A., Barkana R., 2016, MNRAS, 459, L90
DeBoer D. R. et al., 2017, PASP, 129, 974
Ewall-Wice A. et al., 2016, MNRAS, 460, 4320
Fialkov A., 2014, Int. J. Mod. Phys. D, 23, 1430017
Fialkov A., Barkana R., 2014, MNRAS, 445, 213
Fialkov A., Loeb A., 2016, ApJ, 821, 59
Fialkov A., Barkana R., Tseliakhovich D., Hirata C. M., 2012, MNRAS, 424, 1335
Fialkov A., Barkana R., Visbal E., Tseliakhovich D., Hirata C. M., 2013, MNRAS, 432, 2909
Fialkov A., Barkana R., Visbal E., 2014, Nature, 506, 197
Fialkov A., Cohen A., Barkana R., Silk J., 2017, MNRAS, 464, 3498
Field G. B., 1958, PIRE, 46, 240
Fragos T., Lehmer B. D., Naoz S., Zezas A., Basu-Zych A., 2013, ApJ, 776, L31
Furlanetto S. R., 2006, MNRAS, 371, 867
Furlanetto S. R., Oh S. P., Briggs F. H., 2006, PhR 433, 181
Furlanetto S. R., Zaldarriaga M., Hernquist L., 2004, ApJ, 613, 1
Gilfanov M., Grimm H.-J., Sunyaev R., 2004, MNRAS, 347, 57
Greig B., Mesinger A., 2015, MNRAS, 449, 4246
Grimm H.-J., Gilfanov M., Sunyaev R., 2003, MNRAS, 339, 793

Gunn J. E., Peterson B. A., 1965, ApJ, 142, 1633
Haiman Z., Rees M. J., Loeb A., 1997, ApJ, 476, 458; erratum 484, 985
Harker G. J. A., Mirocha J., Burns J. O., Pritchard J. R., 2016, MNRAS, 455, 3829
Iliev I. T., Mellema G., Pen U.-L., Merz H., Shapiro P. R., Alvarez M. A., 2006, MNRAS, 369, 1625
Jeon M., Pawlik A. H., Bromm V., Milosavljevic M., 2014, MNRAS, 444, 3288
Koopmans L. et al., 2015, Proceedings of Advancing Astrophysics with the Square Kilometre Array (AASKA14), 2014 June 9–13, Giardini Naxos, Italy
Lehmer B. D. et al., 2012, ApJ, 752, 46
Leitherer C. et al., 1999, ApJS, 123, 3
Machacek M. E., Bryan G. L., Abel T., 2001, ApJ, 548, 509
Madau P., Fragos A., 2017, ApJ, 840, 39
Madau P., Meiksin A., Rees M. J., 1997, ApJ, 475, 429
Madau P., Rees M. J., Volonteri M., Haardt F., Oh S. P., 2004, ApJ, 604, 484
Mashian N., Oesch P. A., Loeb A., 2016, MNRAS, 455, 2101
Mason C. A., Trenti M., Treu T., 2015, ApJ, 813, 21
Mesinger A., Furlanetto S., Cen R., 2011, MNRAS, 411, 955
Mesinger A., Greig B., Sobacchi E., 2016, MNRAS, 459, 2342
Mineo S., Gilfanov M., Sunyaev R., 2012, MNRAS, 419, 2095
Mirabel I. F., Dijkstra M., Laurent P., Loeb A., Pritchard J. R., 2011, A&A, 528, 149
Mirocha J., Harker G. J. A., Burns J. O., 2013, ApJ, 777, 118
Mirocha J., Harker G. J. A., Burns J. O., 2015, ApJ, 813, 11
Mirocha, Furlanetto S. R., Sun G., 2017, MNRAS, 464, 1365
Naoz S., Barkana R., 2006, MNRAS, 373, 98
O'Shea B. W., Wise J. H., Xu H., Norman M. L., 2015, ApJ, 807, 12
Oh S. P., 2001, ApJ, 553, 499
Patra N., Subrahmanyan R., Raghunathan A., Udaya Shankar N., 2013, ExA, 36, 319
Planck Collaboration et al., 2014, A&A, 571, A16
Planck Collaboration et al., 2016a, A&A, 594, A13
Planck Collaboration et al., 2016b, A&A, 596, A108
Planck Collaboration et al., 2016c, A&A, 596, A107
Pober J. C. et al., 2014, ApJ, 782, 66
Pober J. C. et al., 2015, ApJ, 809, 62
Press W. H., Schechter P., 1974, ApJ, 187, 425
Read J. I., Iorio G., Agertz O., Fraternali F., 2017, MNRAS, 467, 2019
Schauer A. T. P., Whalen D. J., Glover S. C. O., Klessen R. S., 2015, MNRAS, 454, 2441
Sobacchi E., Mesinger A., 2013, MNRAS, 432, 3340
Sun G., Furlanetto S. R., 2016, MNRAS, 460, 417
Tanaka T., Perna R., Haiman Z., 2012, MNRAS, 425, 2974
Tegmark M., Silk J., Rees M., Blanchard A., Abel T., Palla F., 1997, ApJ, 474, 1
Tinker J. L. et al., 2017, ApJ, 839, 121
Tseliakhovich D., Hirata C. M., 2010, PRD, 82, 3520
Tseliakhovich D., Barkana R., Hirata C. M., 2011, MNRAS, 418, 906
van Haarlem M. P. et al., 2013, A&A, 556, 2
Visbal E., Barkana R., Fialkov A., Tseliakhovich D., Hirata C. M., 2012, Nature, 487, 70
Visbal E., Zoltan H., Terrazas B., Bryan G. L., Barkana R., 2014, MNRAS, 445, 107
Wise J. H., Demchenko V. G., Halicek M. T., Norman M. L., Turk M. J., Abel T., Smith B. D., 2014, MNRAS, 442, 2560
Wouthuysen S. A., 1952, AJ, 57, 31
Wyithe J. S. B., Loeb A., 2003, ApJ, 595, 614
Wyithe J. S. B., Loeb A., 2004, Nature, 432, 194
Wyithe J. S. B., Loeb A., 2013, MNRAS, 428, 2741
Xu H., Wise J. H., Norman M. L., Ahn K., O'Shea B. W., 2016, ApJ, 833, 84
Yoshida N., Abel T., Hernquist L., Sugiyama N., 2003, ApJ, 592, 645

APPENDIX: CASES LIST

Table A1. List of the parameter sets used in this paper.

#		f_*	V_c (km s^{-1})	f_X	SED	τ	LW	Low-mass cut-off	ζ	$R_{\rm mfp}$ (Mpc)
1	Filler	0.005	4.2	0.1	Hard	0.066	On	Equation (4)	20	70
2	Filler	0.005	4.2	0.1	Hard	0.082	On	Equation (4)	32	70
3	Filler	0.005	4.2	0.1	Soft	0.066	On	Equation (4)	20	70
4	Filler	0.005	4.2	0.1	Soft	0.082	On	Equation (4)	32	70
5	Filler	0.005	4.2	1	Hard	0.066	On	Equation (4)	20	70
6	Filler	0.005	4.2	1	Hard	0.082	On	Equation (4)	32	70
7	Filler	0.005	4.2	1	Soft	0.066	On	Equation (4)	20	70
8	Filler	0.005	4.2	1	Soft	0.082	On	Equation (4)	32	70
9	Filler	0.005	4.2	8	Hard	0.066	On	Equation (4)	20	70
10	Filler	0.005	4.2	8	Hard	0.082	On	Equation (4)	32	70
11	Filler	0.005	4.2	8	Soft	0.066	On	Equation (4)	19	70
12	Filler	0.005	4.2	8	Soft	0.082	On	Equation (4)	31	70
13	Filler	0.05	4.2	0.1	Hard	0.066	On	Equation (4)	20	70
14	Filler	0.05	4.2	0.1	Hard	0.082	On	Equation (4)	36	70
15	Filler	0.05	4.2	0.1	Soft	0.066	On	Equation (4)	20	70
16	Filler	0.05	4.2	0.1	Soft	0.082	On	Equation (4)	36	70
17	Filler	0.05	4.2	1	Hard	0.066	On	Equation (4)	20	70
18	Filler	0.05	4.2	1	Hard	0.082	On	Equation (4)	36	70
19	Filler	0.05	4.2	1	Soft	0.066	On	Equation (4)	19	70
20	Filler	0.05	4.2	1	Soft	0.082	On	Equation (4)	35	70
21	Filler	0.05	4.2	8	Hard	0.066	On	Equation (4)	18	70
22	Filler	0.05	4.2	8	Hard	0.082	On	Equation (4)	34	70
23	Filler	0.05	4.2	8	Soft	0.066	On	Equation (4)	15	70
24	Filler	0.05	4.2	8	Soft	0.082	On	Equation (4)	31	70
25	Filler	0.5	4.2	0.1	Hard	0.066	On	Equation (4)	26	70
26	Filler	0.5	4.2	0.1	Hard	0.082	On	Equation (4)	51	70
27	Filler	0.5	4.2	0.1	Soft	0.066	On	Equation (4)	25	70
28	Filler	0.5	4.2	0.1	Soft	0.082	On	Equation (4)	51	70
29	Filler	0.5	4.2	1	Hard	0.066	On	Equation (4)	24	70
30	Filler	0.5	4.2	1	Hard	0.082	On	Equation (4)	50	70
31	Filler	0.5	4.2	1	Soft	0.066	On	Equation (4)	20	70
32	Filler	0.5	4.2	1	Soft	0.082	On	Equation (4)	44	70
33	Filler	0.5	4.2	8	Hard	0.066	On	Equation (4)	16	70
34	Filler	0.5	4.2	8	Hard	0.082	On	Equation (4)	39	70
35	Filler	0.5	4.2	8	Soft	0.066	On	Equation (4)	1.5	70
36	Filler	0.5	4.2	8	Soft	0.082	On	Equation (4)	19	70
37	Filler	0.005	16.5	0.1	Hard	0.066	–	–	20	70
38	Filler	0.005	16.5	0.1	Hard	0.082	–	–	37	70
39	Filler	0.005	16.5	0.1	Soft	0.066	–	–	20	70
40	Filler	0.005	16.5	0.1	Soft	0.082	–	–	37	70
41	Filler	0.005	16.5	1	Hard	0.066	–	–	20	70
42	Filler	0.005	16.5	1	Hard	0.082	–	–	37	70
43	Filler	0.005	16.5	1	Soft	0.066	–	–	20	70
44	Filler	0.005	16.5	1	Soft	0.082	–	–	36	70
45	Filler	0.005	16.5	8	Hard	0.066	–	–	20	70
46	Filler	0.005	16.5	8	Hard	0.082	–	–	36	70
47	Filler	0.005	16.5	8	Soft	0.066	–	–	19	70
48	Filler	0.005	16.5	8	Soft	0.082	–	–	36	70
49	Filler	0.05	16.5	0.1	Hard	0.066	–	–	20	70
50	Filler	0.05	16.5	0.1	Hard	0.082	–	–	37	70
51	Filler	0.05	16.5	0.1	Soft	0.066	–	–	20	70
52	Filler	0.05	16.5	0.1	Soft	0.082	–	–	36	70
53	Standard	0.05	16.5	1	Hard	0.066	–	–	20	70
54	Filler	0.05	16.5	1	Hard	0.082	–	–	36	70
55	Filler	0.05	16.5	1	Soft	0.066	–	–	19	70
56	Filler	0.05	16.5	1	Soft	0.082	–	–	36	70
57	Filler	0.05	16.5	8	Hard	0.066	–	–	19	70
58	Filler	0.05	16.5	8	Hard	0.082	–	–	35	70
59	Filler	0.05	16.5	8	Soft	0.066	–	–	15	70
60	Filler	0.05	16.5	8	Soft	0.082	–	–	31	70
61	Filler	0.5	16.5	0.1	Hard	0.066	–	–	20	70
62	Filler	0.5	16.5	0.1	Hard	0.082	–	–	36	70
63	Filler	0.5	16.5	0.1	Soft	0.066	–	–	19	70
64	Filler	0.5	16.5	0.1	Soft	0.082	–	–	36	70

Table A1 *– continued*

#		f_*	V_c (km s^{-1})	f_X	SED	τ	LW	Low-mass cut-off	ζ	$R_{\rm mfp}$ (Mpc)
65	Filler	0.5	16.5	1	Hard	0.066	–	–	18	70
66	Filler	0.5	16.5	1	Hard	0.082	–	–	35	70
67	Filler	0.5	16.5	1	Soft	0.066	–	–	14	70
68	Filler	0.5	16.5	1	Soft	0.082	–	–	30	70
69	Filler	0.5	16.5	8	Hard	0.066	–	–	11.5	70
70	Filler	0.5	16.5	8	Hard	0.082	–	–	27	70
71	Filler	0.5	16.5	8	Soft	0.066	–	–	0.01	70
72	Filler	0.5	16.5	8	Soft	0.082	–	–	9	70
73	Filler	0.005	35.5	0.1	Hard	0.082	–	–	130	70
74	Filler	0.005	35.5	0.1	Soft	0.066	–	–	53	70
75	Filler	0.005	35.5	0.1	Soft	0.082	–	–	130	70
76	Filler	0.005	35.5	1	Hard	0.066	–	–	53	70
77	Filler	0.005	35.5	1	Hard	0.082	–	–	130	70
78	Filler	0.005	35.5	1	Soft	0.066	–	–	53	70
79	Filler	0.005	35.5	1	Soft	0.082	–	–	130	70
80	Filler	0.005	35.5	8	Hard	0.066	–	–	53	70
81	Filler	0.005	35.5	8	Hard	0.082	–	–	130	70
82	Filler	0.005	35.5	8	Soft	0.066	–	–	53	70
83	Filler	0.005	35.5	8	Soft	0.082	–	–	129	70
84	Filler	0.05	35.5	0.1	Hard	0.066	–	–	53	70
85	Filler	0.05	35.5	0.1	Hard	0.082	–	–	130	70
86	Filler	0.05	35.5	0.1	Soft	0.066	–	–	53	70
87	Filler	0.05	35.5	0.1	Soft	0.082	–	–	130	70
88	Filler	0.05	35.5	1	Hard	0.066	–	–	53	70
89	Filler	0.05	35.5	1	Hard	0.082	–	–	130	70
90	Filler	0.05	35.5	1	Soft	0.066	–	–	52	70
91	Filler	0.05	35.5	1	Soft	0.082	–	–	129	70
92	Filler	0.05	35.5	8	Hard	0.066	–	–	52	70
93	Filler	0.05	35.5	8	Hard	0.082	–	–	129	70
94	Filler	0.05	35.5	8	Soft	0.066	–	–	48	70
95	Filler	0.05	35.5	8	Soft	0.082	–	–	124	70
96	Filler	0.5	35.5	0.1	Hard	0.066	–	–	53	70
97	Filler	0.5	35.5	0.1	Hard	0.082	–	–	130	70
98	Filler	0.5	35.5	0.1	Soft	0.066	–	–	52	70
99	Filler	0.5	35.5	0.1	Soft	0.082	–	–	129	70
100	Filler	0.5	35.5	1	Hard	0.066	–	–	52	70
101	Filler	0.5	35.5	1	Hard	0.082	–	–	129	70
102	Filler	0.5	35.5	1	Soft	0.066	–	–	47	70
103	Filler	0.5	35.5	1	Soft	0.082	–	–	122	70
104	Filler	0.5	35.5	8	Hard	0.066	–	–	43	70
105	Filler	0.5	35.5	8	Hard	0.082	–	–	119	70
106	Filler	0.5	35.5	8	Soft	0.066	–	–	22	70
107	Filler	0.5	35.5	8	Soft	0.082	–	–	91	70
108	Large	0.5	4.2	10	MQ	0.098	Off	Equation (3)	27	70
109	Large	0.5	4.2	0.1	Soft	0.098	Off	Equation (3)	26	70
110	Large	0.5	4.2	0.1	MQ	0.098	Off	Equation (3)	28	70
111	Large	0.005	4.2	10	Soft	0.098	Off	Equation (3)	26	70
112	Large	0.005	4.2	10	MQ	0.098	Off	Equation (3)	27	70
113	Large	0.005	4.2	0.1	Soft	0.098	Off	Equation (3)	28	70
114	Large	0.005	4.2	0.1	MQ	0.098	Off	Equation (3)	28	70
115	Large	0.5	76.5	10	Soft	0.066	–	–	387	70
116	Large	0.5	76.5	10	Soft	0.098	–	–	6000	70
117	Large	0.5	76.5	10	MQ	0.066	–	–	450	70
118	Large	0.5	76.5	10	MQ	0.098	–	–	6060	70
119	Large	0.5	76.5	0.1	Soft	0.066	–	–	455	70
120	Large	0.5	76.5	0.1	Soft	0.098	–	–	6060	70
121	Large	0.5	76.5	0.1	MQ	0.098	–	–	6060	70
122	Large	0.016	76.5	10	Soft	0.066	–	–	455	70
123	Large	0.16	76.5	10	Soft	0.098	–	–	6060	70
124	Large	0.016	76.5	10	MQ	0.066	–	–	455	70
125	Large	0.16	76.5	10	MQ	0.098	–	–	6060	70
126	Large	0.16	76.5	0.1	Soft	0.098	–	–	6060	70
127	Large	0.16	76.5	0.1	MQ	0.098	–	–	6060	70

Table A1 – *continued*

#		f_*	V_c (km s^{-1})	f_X	SED	τ	LW	Low-mass cut-off	ζ	$R_{\rm mfp}$ (Mpc)
128	Small	0.16	4.2	3.16	Hard & MQ	0.066	On	Equation (4)	21	70
129	Small	0.16	4.2	3.16	Hard & MQ	0.082	On	Equation (4)	41	70
130	Small	0.16	4.2	3.16	Soft & MQ	0.066	On	Equation (4)	18	70
131	Small	0.16	4.2	3.16	Soft & MQ	0.082	On	Equation (4)	38	70
132	Small	0.16	4.2	0.32	Hard & MQ	0.066	On	Equation (4)	21	70
133	Small	0.16	4.2	0.32	Hard & MQ	0.082	On	Equation (4)	42	70
134	Small	0.16	4.2	0.32	Soft & MQ	0.066	On	Equation (4)	21	70
135	Small	0.16	4.2	0.32	Soft & MQ	0.082	On	Equation (4)	42	70
136	Small	0.016	4.2	3.16	Hard & MQ	0.066	On	Equation (4)	20	70
137	Small	0.016	4.2	3.16	Hard & MQ	0.082	On	Equation (4)	33	70
138	Small	0.016	4.2	3.16	Soft & MQ	0.066	On	Equation (4)	19	70
139	Small	0.016	4.2	3.16	Soft & MQ	0.082	On	Eequation (4)	33	70
140	Small	0.016	4.2	0.32	Hard & MQ	0.066	On	Equation (4)	20	70
141	Small	0.016	4.2	0.32	Hard & MQ	0.082	On	Equation (4)	33	70
142	Small	0.016	4.2	0.32	Soft & MQ	0.066	On	Equation (4)	20	70
143	Small	0.016	4.2	0.32	Soft & MQ	0.082	On	Equation (4)	33	70
144	Small	0.16	35.5	3.16	Hard & MQ	0.066	–	–	52	70
145	Small	0.16	35.5	3.16	Hard & MQ	0.082	–	–	129	70
146	Small	0.16	35.5	3.16	Soft & MQ	0.066	–	–	49	70
147	Small	0.16	35.5	3.16	Soft & MQ	0.082	–	–	126	70
148	Small	0.16	35.5	0.32	Hard & MQ	0.066	–	–	53	70
149	Small	0.16	35.5	0.32	Hard & MQ	0.082	–	–	130	70
150	Small	0.16	35.5	0.32	Soft & MQ	0.066	–	–	53	70
151	Small	0.16	35.5	0.32	Soft & MQ	0.082	–	–	130	70
152	Small	0.016	35.5	3.16	Hard & MQ	0.066	–	–	53	70
153	Small	0.016	35.5	3.16	Hard & MQ	0.082	–	–	130	70
154	Small	0.016	35.5	3.16	Soft & MQ	0.066	–	–	53	70
155	Small	0.016	35.5	3.16	Soft & MQ	0.082	–	–	130	70
156	Small	0.016	35.5	0.32	Hard & MQ	0.066	–	–	53	70
157	Small	0.016	35.5	0.32	Hard & MQ	0.082	–	–	130	70
158	Small	0.016	35.5	0.32	Soft & MQ	0.066	–	–	53	70
159	Small	0.016	35.5	0.32	Soft & MQ	0.082	–	–	130	70
160	Fialkov et al. (2017)	0.05	16.5	1	MQ	0.0738	–	–	24	70
161	Fialkov et al. (2017)	0.05	16.5	1	MQ	0.0956	–	–	57	70
162	Fialkov et al. (2017)	0.05	16.5	10.8	Hard	0.0756	–	–	24	70
163	Fialkov et al. (2017)	0.05	16.5	29.5	Soft	0.0859	–	–	24	70
164	Fialkov et al. (2017)	0.05	16.5	11.4	MQ	0.0747	–	–	24	70
165	Fialkov et al. (2017)	0.05	16.5	44.4	Hard	0.0990	–	–	57	70
166	Fialkov et al. (2017)	0.05	16.5	102	Soft	0.1111	–	–	57	70
167	Fialkov et al. (2017)	0.05	16.5	74.4	MQ	0.0977	–	–	57	70
168	Fialkov et al. (2017)	0.05	16.5	0.01	Hard	0.0739	–	–	24	70
169	Fialkov et al. (2017)	0.05	16.5	0.0023	Soft	0.0746	–	–	24	70
170	Fialkov et al. (2017)	0.05	16.5	0	Hard	0.0957	–	–	57	70
171	Fialkov et al. (2017)	0.05	35.5	1	MQ	0.0597	–	–	32	70
172	Fialkov et al. (2017)	0.05	35.5	1	MQ	0.0831	–	–	112	70
173	Fialkov et al. (2017)	0.05	35.5	14.7	Hard	0.0609	–	–	32	70
174	Fialkov et al. (2017)	0.05	35.5	41.4	Soft	0.0688	–	–	32	70
175	Fialkov et al. (2017)	0.05	35.5	12.1	MQ	0.0606	–	–	32	70
176	Fialkov et al. (2017)	0.05	35.5	79.2	Hard	0.0850	–	–	112	70
177	Fialkov et al. (2017)	0.05	35.5	188	Soft	0.0934	–	–	112	70
178	Fialkov et al. (2017)	0.05	35.5	87.9	MQ	0.0847	–	–	112	70
179	Fialkov et al. (2017)	0.05	35.5	0	Hard	0.0831	–	–	112	70
180	Fialkov et al. (2017)	0.05	35.5	0.036	Hard	0.0597	–	–	32	70
181	Fialkov et al. (2017)	0.05	35.5	0.0095	Soft	0.0601	–	–	32	70
182	$R_{\rm mfp}$	0.005	35.5	0.1	Hard	0.082	–	–	125	20
183	$R_{\rm mfp}$	0.005	35.5	0.1	Soft	0.082	–	–	125	20
184	$R_{\rm mfp}$	0.005	35.5	1	Hard	0.082	–	–	125	20
185	$R_{\rm mfp}$	0.05	35.5	0.1	Hard	0.082	–	–	125	20
186	$R_{\rm mfp}$	0.5	76.5	0.1	Hard	0.066	–	–	389	20
187	$R_{\rm mfp}$	0.5	76.5	0.1	Hard	0.082	–	–	1411	20
188	$R_{\rm mfp}$	0.005	35.5	0.1	Hard	0.082	–	–	202	5
189	$R_{\rm mfp}$	0.005	35.5	0.1	Soft	0.082	–	–	202	5
190	$R_{\rm mfp}$	0.005	35.5	1	Hard	0.082	–	–	202	5
191	$R_{\rm mfp}$	0.05	35.5	0.1	Hard	0.082	–	–	202	5
192	$R_{\rm mfp}$	0.5	76.5	0.1	Hard	0.066	–	–	1172	5
193	$R_{\rm mfp}$	0.5	76.5	0.1	Hard	0.082	–	–	6125	5

This paper has been typeset from a TEX/LATEX file prepared by the author.